THE SAMPLE COMPLEXITY OF QUANTUM ENTANGLEMENT ALLOCATION

Anonymous authors
Paper under double-blind review

ABSTRACT

How many past requests are needed to decide which qubits should share entanglement? We show that the answer depends on the allocation choices created by the queries: a larger memory can require no more data. The memory stores a classical bit and answers requests through a fixed detector that preserves coherence within each measured sector. For independent commuting X- and Z-type Pauli queries, we characterize the full attainable prediction-contrast region and construct encodings that preserve the bit at every nonzero vertex. With sharp reports, a d-qubit path and groups of at most k qubits have minimax excess error after m requests proportional to $k^{-1}\min\{1, \sqrt{d\log(k+1)/m}\}$, uniformly for $2 \le k < d$. Connected biclique regions can grow without increasing sample demand when depth, region count and connections per region stay bounded. Preparation noise introduces a separate calibration requirement. We derive an exact tradeoff with extra fresh detector calls and transfer the learning law to structured transaction co-location. Population-risk experiments test the statistical predictions. We also compare encodings on a native 15-qubit device and learned partitions on public purchase baskets. The full chain wins on the device; frequency grouping outperforms basket search in the largest-capacity retail setting.

1 INTRODUCTION

A quantum memory is prepared before the request it must answer is known. When different requests favor different groups of entangled qubits, the encoder has to choose where to spend its entanglement budget. We ask how many past requests it needs to make that choice.

The choice matters even when the memory stores just one classical bit. Consider a three-qubit memory queried through ZZI, XXX and IZZ, with probabilities $1/4$, $1/2$ and $1/4$. A product code supports both Z parities perfectly, but its X parity is uninformative. With groups capped at two qubits, entangling the first pair supports ZZI and XXX, reducing optimal prediction error from 25% to 12.5%. Both memories retain the bit without loss. What changes is which requests they can answer. The request frequencies determine which pair is better (Figure 1). The encoder learns how to arrange information it already has.

The detector determines which arrangements are useful. We consider a supplied parity detector that preserves arbitrary coherence within each parity sector, as required of an ideal native parity measurement (Ristè et al., 2013). Measuring individual qubits and combining their outcomes can reveal the parity, but destroys this coherence. We hold the detector fixed and vary the entanglement in the stored state.

Our answer depends on the choices created by the query geometry. For independent commuting X- and Z-type Pauli queries, we characterize the attainable prediction contrasts under arbitrary allowed partition mixtures (Theorem 1). This reduces learning over all allowed encoders, including mixed states, to learning which query sets to support. Paths add choices as they grow; boundedly connected biclique regions can grow without adding to the sample requirement (Theorem 2).

Imperfect preparation also makes calibration necessary. We study the request and calibration budgets, price the extra detector calls that can replace entangled preparation, and transfer the learning law to classical transaction co-location.

Reviewers: please read the Reviewer Guidelines (iclr.cc/Conferences/2027/ReviewerGuidelines) and the AI Policy for Reviewers (iclr.cc/Conferences/2027/AIPolicyForReviewers). If you used AI to expand, edit, or polish your review, please provide the input text to the LLM. Better still, consider skipping the LLM and submitting your original text: we, and the authors, are much more interested in your unedited thoughts than in what an LLM has to say. AI-assisted or not, you are putting your name and reputation behind your review: LLM-generated falsehoods, hallucinations or misrepresentations are subject to disciplinary action, which may include desk-rejecting all papers you have authored.

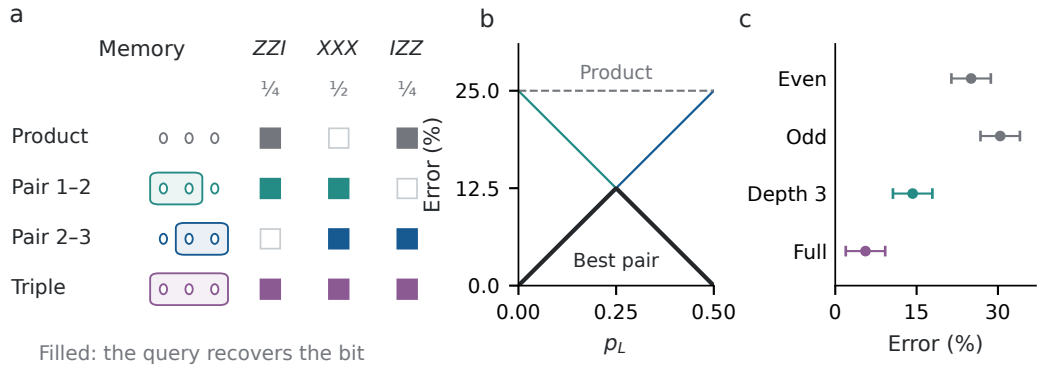

Figure 1: (a) Three-qubit encodings at request probabilities $(1/4, 1/2, 1/4)$. Groups share entanglement; filled squares recover the bit, empty squares are uninformative. All four codes preserve the stored bit. (b) Ideal prediction error when $\pi(XXX) = 1/2$, $\pi(ZZI) = p_L$ and $\pi(IZZ) = 1/2 - p_L$; black selects the better pair. (c) Native 15-qubit commissioning on `ibm_marrakesh` favors the full chain. Even/odd are fixed product allocations. Each mean uses 1,920 shots over all 15 queries and both bits; bars are simultaneous 95% Hoeffding bounds for four means, conditional on independent shots in this one job. The allocations in (c) are fixed before acquisition.

2 The memory and its detector

Let C be uniform on $\{0, 1\}$ and let $G = C \oplus Z$, with independent $Z \sim \text{Bernoulli}(h)$ and $0 \leq h < 1/2$. Write $D = 1 - 2h$. An encoder receives G, prepares a d-qubit state τ_G, and discards its classical record and environment. An independent request $T = t$ arrives with probability π_t. The decoder receives t and the detector's classical report, and predicts C. It has no additional copy, correlated input or later unrestricted measurement.

Given a collection $\mathcal{F}$ of allowed qubit partitions, let $\mathcal{S}_{\mathcal{F}}$ be the convex hull of states product across a partition in $\mathcal{F}$. Both codewords belong to this class, but may use different partitions and mixtures. Allowing every partition with blocks of size at most k gives an entanglement-depth constraint. The same collective detector is available to every encoder; k constrains the stored state, not the detector's subsequent operations.

Orthogonal codeword supports preserve G: a global measurement recovers it, giving unrestricted error h and information $1 - H_2(h)$ bits about C. The optimization allows information-losing codes. We will show that an optimum can always preserve the bit.

2.1 Which reports preserve a parity sector?

For a requested Hermitian Pauli observable P, put $\Pi_\pm = (I \pm P)/2$. The detector's nonselective system channel must be

$$\mathcal{L}_P(\rho) = \Pi_+ \rho \Pi_+ + \Pi_- \rho \Pi_- . \tag{1}$$

This Lüders channel preserves all coherence within each sector. An individual-outcome refinement can preserve the parity eigenvalue while violating Eq. (1).

Every instrument summing to $\mathcal{L}_P$ has outcome effects $E_y = q(y|+)\Pi_+ + q(y|-)\Pi_-$ for a stochastic matrix q. Thus the report contains only a postprocessed parity, however large its alphabet. This follows from channel–measurement compatibility (Heinosaari & Miyadera, 2013); Appendix A gives a short proof and an approximate version. The all-input requirement matters: a shared syndrome service must preserve unknown coherent inputs even when a particular client stores a classical bit.

We first use sharp parity reports. Symmetric, code-independent report noise gives effects $(I \pm v_t P_t)/2$, with known $v_t \in [0, 1]$. For contrast $c_t = |\operatorname{Tr}[P_t(\tau_0 - \tau_1)]|/2$, the optimal classical

decoder has risk

$$R = \frac{1}{2} - \frac{D}{2} \sum_t \pi_t v_t c_t. \tag{2}$$

Small departures from exact channel preservation can also be bounded: Appendix A gives a dimension-independent continuity bound and a sufficient diamond-distance threshold for the separation. Under the exact contract, the remaining task is to determine which contrast vectors fit the entanglement budget.

3 WHICH QUERIES CAN AN ENCODING SUPPORT?

Queries that commute globally can compete within separate qubit groups. Consider independent, globally commuting Pauli generators $P_1, \ldots, P_q$. Independence means no nonempty product is proportional to the identity. A CSS family uses only X and identity within each X-type generator, and only Z and identity within each Z-type generator. For a partition Π, build a graph H_Π on queries: two queries are adjacent when their restrictions anticommute on a block. This graph is bipartite, since generators of the same CSS type cannot conflict. Let $\mathrm{STAB}(H)$ be the convex hull of independent-set indicators, including the empty set.

To characterize the contrasts, we first reduce a pair of codewords to one state. A tensor product of single-qubit Paulis flips all independent generators at once and preserves every partition class. Binary contrasts therefore have the same attainable region as single-state absolute correlations (Appendix B).

Theorem 1 (Exact attainable contrast region)**.** *For independent commuting CSS generators and any partition family $\mathcal{F}$, the contrast vectors of all pairs $\tau_0, \tau_1 \in \mathcal{S}_\mathcal{F}$ are exactly*

$$\mathcal{C}_\mathcal{F} = \mathrm{conv} \bigcup_{\Pi \in \mathcal{F}} \mathrm{STAB}(H_\Pi). \tag{3}$$

Every nonempty independent-set indicator has an explicit encoding with orthogonal supports in the allowed class.

Local uncertainty bounds each conflicting pair by $|\langle P_u \rangle| + |\langle P_v \rangle| \leq 1$ (Zander & Becker, 2025, Proposition A.3). Bipartite integrality and convexity turn these pairwise inequalities into an upper bound on the whole region, including mixed codeword pairs. To attain the bound, take an independent set I and define

$$\tau_g^I = 2^{-d} \prod_{t \in I} \left(\mathbb{I} + (-1)^g P_t\right) \tag{4}$$

where $\mathbb{I}$ is the identity. This normalized stabilizer projector is separable across the chosen partition and has $c = \mathbf{1}_I$. Every selected expectation has sign $(-1)^g$. Mixing the pairs thus adds their contrasts without cancellation and fills the region in Eq. (3). Each nonempty pair preserves G, although a mixture of such pairs need not do so.

With $a_t = \pi_t v_t$, the optimal risk is $1/2 - (D/2) \max_{\Pi \in \mathcal{F}} \alpha_a(H_\Pi)$, where α_a is maximum independent-set weight. The workload objective is linear, so a best vertex is optimal and its encoding preserves the bit. Mixtures can enlarge the feasible region without improving this optimum. Appendix B gives the proof and counterexamples to dropping CSS or independence; the extended supplement gives a worked lossless mixture.

3.1 WHICH QUBITS SHOULD SHARE ENTANGLEMENT?

For graph-state queries, the contrast region becomes a concrete allocation problem. A bipartite graph has generators $K_i = X_i \prod_{j \sim i} Z_j$; Hadamards on one color convert them to CSS form. The conflict graph contains exactly the edges crossing the partition. Weighted bipartite vertex cover then gives the following rule. Delete a minimum-weight set of query vertices until every remaining connected component has at most k vertices, and entangle within those components. A deleted vertex means giving up a query; its qubit stays in the memory. This is a variant of classical component-order connectivity (Drange et al., 2016): deletion costs carry workload weights, while the surviving-component limit counts vertices.

With sharp reports, error h is attainable exactly when every connected component of the positive-weight query graph fits the budget. For a uniform d-vertex path,

$$R_k^* = h + \frac{D}{2d}\left\lfloor \frac{d}{k+1} \right\rfloor. \tag{5}$$

Exact recovery of G through every query requires depth d. Constant-size groups suffice for a fixed excess error independent of d. Each path query touches at most three qubits, so independent local outcome errors introduce at most three visibility factors.

4 Learning where entanglement belongs

The allocation rule assumes that the request frequencies are known. We now give the learner only m i.i.d. past query identities. It chooses an encoding before future requests arrive and receives no prediction labels. For a known bipartite graph Γ and its graph-state queries, let $R^*_{\pi,k}$ be the best depth-k risk for workload π, and define $\mathfrak{M}_m(\Gamma, k) = \inf_{\widehat{\tau}} \sup_{\pi} \mathbb{E}[R_\pi(\widehat{\tau}) - R^*_{\pi,k}]$. The supremum ranges over all query distributions. The m query identities are the learner's only observations.

We learn the allocation by maximizing empirical workload weight over *inclusion-maximal* feasible query sets: no further query can be added while preserving feasibility. Restricting to these sets preserves every nonnegative workload optimum, and each set specifies an explicit lossless code. With at most 2^q feasible indicators, finite-class concentration gives excess error $O(D\sqrt{(q + \log(1/\delta))/m})$ with probability $1 - \delta$. This finite-class bound assumes exact empirical optimization, which can remain combinatorial. To sharpen it, we need to count the undominated allocation choices that the requests must distinguish.

In the opening example, the choice is which endpoint to pair with the center. Local graph queries can create proportionally more such choices as the memory grows. A complete bipartite graph $K_{a,b}$ has a different structure. At depth $k \le \min(a, b)$, a retained set either lies in one color or has at most k vertices. The maximal sets are the two full colors and mixed sets of size k, so the oracle compares the color totals with the sum of the k largest weights.

To separate the number of regions from their size, divide a bipartite graph into r complete-bipartite regions, linked through at most p designated connection vertices per region. Each color must have at least k nonconnection vertices. Regions may have different sizes, and physical blocks may cross their boundaries. The following result compares this family with bounded-degree graphs.

Theorem 2 (Geometry and the cost of allocation learning)**.** *Assume sharp reports and $m \ge 1$ i.i.d. query samples. On a path with $d \ge 3$ vertices and $2 \le k \le d-1$,*

$$\mathfrak{M}_m(P_d, k) = \Theta\left(\frac{D}{k}\min\left\{1, \sqrt{\frac{d\log(k+1)}{m}}\right\}\right). \tag{6}$$

The constants are uniform in d, k, m. For r biclique regions with fixed connection bound p and at least k nonconnection vertices per color,

$$\mathfrak{M}_m(\Gamma, k) = \Theta_p\Big(D\min\{1, \sqrt{rk/m}\}\Big). \tag{7}$$

The second law is uniform in r, k and the region sizes. A single region without connections recovers $\mathfrak{M}_m(K_{a,b}, k) = \Theta(D\min\{1, \sqrt{k/m}\})$. All partitions within the depth budget are allowed. Both lower bounds permit arbitrary randomized learners choosing mixed codeword pairs and grant the optimal decoder. Information-preserving codes attain both rates. The path learner uses a random periodic allocation at small budgets and empirical maximization at larger budgets; regional empirical maximization attains the second rate. If $d \le k$, the whole graph fits and allocation excess is zero.

On a path, one deletion every $k+1$ sites sacrifices at most $1/(k+1)$ of the workload after averaging over offsets. The resulting small oracle loss lets us sharpen the concentration bound. For the lower bound, separated $(k+1)$-site segments each force a choice of which query to sacrifice; identifying the least requested of $k+1$ alternatives supplies the logarithmic factor (Appendix E). Increasing depth reduces absolute error. Learning a sufficiently small fixed fraction of that error scale still requires

order $d \log(k+1)$ requests. A sliding-minimum recurrence solves the ideal empirical problem in $O(d)$ operations after counting.

The maximal biclique allocation class has VC dimension k, although all feasible sets together have dimension $\max(a, b)$. With r connected regions, interior choices contribute at most rk and connection vertices at most rp. A matching lower bound projects onto r independent capacity constraints, even when physical groups cross regions (Appendix C.3). A chain of regions admits exact empirical optimization in $O(rk^2)$ operations after sorting. Completing empirical ties to maximal sets preserves training weight and weakly improves every nonnegative population objective (Appendix F).

The laws describe worst-case workloads. A fixed workload with a clear gap between competing allocations can be learned faster. Giving every query positive probability leaves the minimax value unchanged unless a common probability floor is imposed. The regional reduction in sample demand also comes with a physical cost: biclique queries grow with the region, whereas bounded-degree queries touch at most $\Delta + 1$ qubits. Paths and chains of regions admit efficient exact empirical optimization; the general graph theorem assumes access to an optimization oracle.

5 Learning allocation under preparation errors

So far, supporting another query can only help. Preparation errors change that tradeoff: the gate that supports one query may reduce its neighbors' reliability. On a path, select vertices S, prepare a graph state on each selected run, and put deleted sites in $|0\rangle$. Encode G by applying Z^G to every selected site. Suppose each retained CZ gate on edge e is independently followed by a ZZ error with probability $\epsilon_e \le 1/2$. With $\gamma_e = 1 - 2\epsilon_e$ and query visibility v_i,

$$b_i(S) = \mathbf{1}\{i \in S\}\, v_i \prod_{\substack{e \ni i \\ e \text{ retained}}} \gamma_e. \tag{8}$$

Here $b_i(S)$ includes reporting visibility, and the risk is $1/2 - (D/2)\sum_i \pi_i b_i(S)$. Retaining an edge changes the value of neighboring queries, so its cost cannot be absorbed into fixed workload weights.

The encoded bit can survive these preparation errors. It is enough to retain one odd-sized component. The product of its stabilizer generators has eigenvalue $(-1)^G$ and commutes with every retained-edge ZZ error. The noisy codewords remain in orthogonal sectors even if other components have even size. An odd full chain also preserves G. A two-site run alone fails because its ZZ error flips the encoded bit.

We optimize within this family by tracking the selected-run length and whether an odd run has closed. The dynamic program uses $O(dk)$ transitions; an independent $O(dk^2)$ interval implementation checks its answers. The noisy optimization is over this lossless circuit family; the ideal theorem optimizes over the full physical class.

Learning this allocation requires information about the device as well as the workload. Suppose we observe m requests and B independent calibration trials for each edge reliability and native query visibility. This statistical model supplies each parameter separately, at a cost of $B(2d-1)$ calibration observations in addition to the request log. Appendix O instead calibrates directly observed binary responses. The comparator is the best allocation in the same noisy circuit family; Appendix G also bounds errors caused by channel mismatch and request smoothing.

The two-resource rate is sharp on depth-three paths. For the same circuit family with $d \ge 4$ and correctly specified noise, the minimax excess from m requests and B trials per parameter is $\Theta\Big(D \min\{1, \sqrt{d/m} + B^{-1/2}\}\Big)$ (Theorem 4). Four-site allocation choices force the request term; two almost indistinguishable three-site channels with different optimal allocations force the calibration term.

6 Experiments

The experiments first test the learning laws under their stated channels, where we can compute population risk exactly. We then test fixed encodings on a quantum processor. The transaction study in Section 7 asks whether allocation learned from a public purchase trace improves locality.

6.1 What changes when the memory grows?

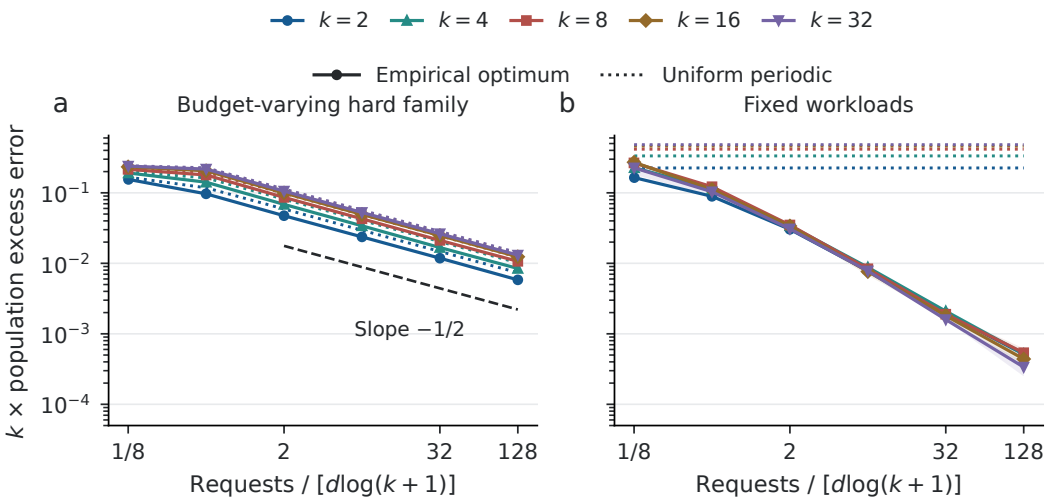

Figure 2: Depth changes the error scale as well as the request requirement. (a) On the budget-indexed hard family, both empirical and data-free periodic allocations follow a square-root rate. The task probabilities change with the budget. (b) On fixed Dirichlet workloads, only the empirical learner improves. Solid lines show empirical optima; dotted lines show uniform periodic allocations. Each line averages four dimension means, each based on 64 independent seeds; shading spans those dimension means, not confidence intervals. The dashed line is $0.025x^{-1/2}$, an unfitted slope guide, not a theorem constant. Every risk uses the exact same-depth physical optimum as comparator.

We varied d from 128 to 1,024 and k from 2 to 32, for 15,360 fits, to test the depth dependence in the path law. Figure 2 scales excess by k and requests by $d\log(k+1)$. Both empirical and data-free allocations follow the hard-family slope because the task probabilities change with the budget. On fixed workloads, the empirical learner improves while the periodic comparator stays flat. The fixed-workload control is essential: a hard-family slope alone would also credit a method that never uses the requests (Appendix H.1).

Connected-region experiments keep the request scale $m/(rk)$ fixed while changing region size. The curves remain similar, as predicted by Theorem 2 (Appendix Figure 6). Empirical ties are completed using training counts alone; retaining only observed queries would introduce an avoidable occupancy penalty. At the original primary condition, selective connection repair plus local improvement is within 0.145 error points of exact optimization (95% interval $[0.075, 0.220]$). The full comparison uses every workload at the same depth (Appendix I).

6.2 Requests and calibration limit different decisions

To test the two-resource prediction, we varied request and calibration budgets separately. The prespecified protocol draws 192 independent workload/channel instances, crossing 63 or 127 qubits with low, heterogeneous or stress preparation noise. Each of the six conditions contains 32 instances, four request streams and four calibration panels. Five nested request budgets and five calibration budgets give 76,800 fits per method. Joint uses requests, edge reliability and report visibility. Task only uses requests; Reporting only also learns visibility. We hold the optimizer and tie rule fixed and compare both raw counts and smoothed estimates to isolate the value of each observation type. Same-family greedy and privileged-oracle controls accompany the full grid (Appendix H).

With $B = 4$, increasing requests from 16 to 4,032 reduces excess from 6.48 to 1.33 points. Even exact workload knowledge leaves 1.30 points of excess, so more requests cannot remove this calibration floor. At $B = 256$, the same request increase reduces excess from 5.26 to 0.085 points. Conversely, at $m = 16$, even 1,024 calibration trials leave 5.14 points: the request estimate is now

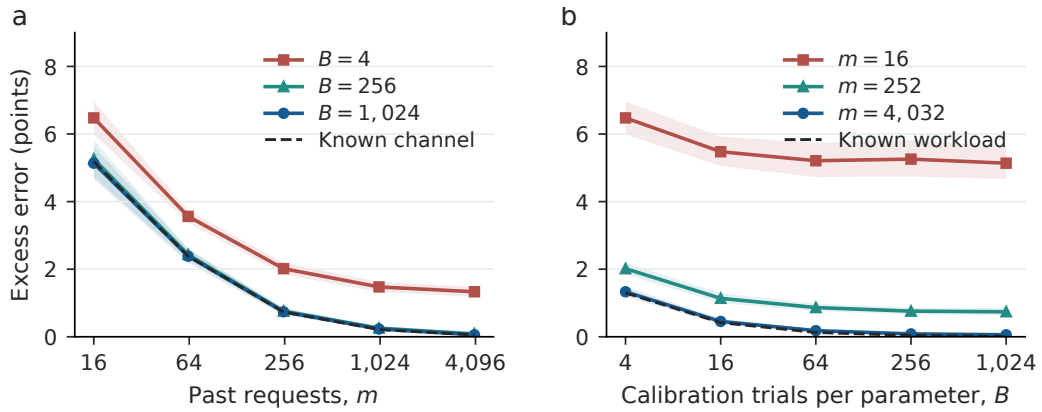

Figure 3: More requests cannot remove a calibration floor. (a) Request learning at three fixed calibration budgets; the dashed curve supplies the true channel. (b) Calibration learning at three fixed request budgets; the dashed curve supplies the true workload. Both panels use 63-qubit heterogeneous-noise instances and the smoothed Joint estimator. Excess is relative to the true-workload, true-channel oracle in the same circuit family. Bands are pointwise 95% bootstrap intervals over 32 independent instances, after averaging four request streams and four calibration panels. Calibration costs $125B$ observations, separately from m.

the bottleneck (Figure 3). The same instances thus exhibit either bottleneck, depending on which data are scarce. A separate near-indifference diagnostic gives approximately constant $\sqrt{B}$-scaled excess over $B = 4$ to 4,096, with workload known.

In the prespecified 63-qubit heterogeneous-noise comparison, 1,008 requests and 256 calibration trials per parameter reduce error from 9.79% for Task only to 8.58% for Joint: a 1.21-point gain, paired 95% interval $[0.95, 1.50]$. Calibration costs 32,000 observations; the learned code uses 22.3 preparation CZs on average, versus 62 for Full chain (Appendix Table 1). These are population risks under the specified channel.

Full chain has lower error in 76 of 150 cells, including every low-noise cell. The benefit of supporting more queries can outweigh their preparation cost. Smoothing affects Joint and Task only differently, so we report all four combinations, along with depth-five and depth-seven sensitivity and same-family greedy comparisons (Appendix H).

6.3 Testing the encodings on a quantum processor

We implement all 15 graph queries on a 15-data-qubit path on `ibm_marrakesh`. Seven query centers have degree two in the device graph. Their parity-extraction circuits borrow data qubits and restore them in the ideal unitary. Dropping those queries would remove the local conflicts that define the learning problem. Preparation and extraction compile separately. Both full and shallow chains use two parallel CZ layers.

In 7,680 commissioning shots, uniform-request error is 5.57% for Full chain, 14.27% for a fixed depth-three allocation, and 25.05% or 30.42% for the two product colors (Figure 1c). The full chain wins this fixed-encoding comparison. Two preliminary learning jobs timed out without usable observations, leaving the four-workload learning/calibration design unmeasured. A separate coherence check also exposed a failure: one witness reverses its expected sign in two jobs, including both bits and phases in the follow-up. The implemented extraction therefore still needs validation across the full path (Appendix N).

7 Consequences of the allocation law

Changing the detector interface. Extra detector calls offer another way to obtain information. We compare their cost with entangled preparation in a common statistical experiment.

For detector diagnosis, a healthy or faulty device independently flips each reported sign with probability $e_0 < e_1$. A supported query gives an observed flip; an unsupported query erases it. Write E_p for this experiment when the supported request mass is p. Appendix K shows that the optimal N-call experiment over all admissible fresh CSS probes is $\mathsf{E}_{p^*}^{\otimes N}$, where p^* is the maximum supported mass. At one call and false-alarm level e_0, power regret is $2(e_1 - e_0)/D$ times prediction regret. Diagnosis inherits the same request-learning laws.

Suppose a competing policy can make additional calls. If each fresh call is dominated by E_p and a fixed probe attains it, reproducing N copies of E_q, $q \geq p$, requires at least Nq/p calls in expectation under either hypothesis. A stopped policy attains equality (Theorem 5). The equality compares expected call budgets for equivalent experiments. Fixed horizons at a specified power can have a different ratio.

For the menu (ZZI, XXX, IZZ) with probabilities $(.2, .6, .2)$, product and Bell coverages are .6 and .8: the fresh-call ratio is $4/3$. If the policy can choose its second query, a product-initialized policy matches Bell at 1.2 expected calls. Retaining the probe and repeating an unsupported query gives yet another signal: the reports disagree with probability $2e_H(1 - e_H)$ in health state H. The disagreement diagnoses noise without recovering the stored sign.

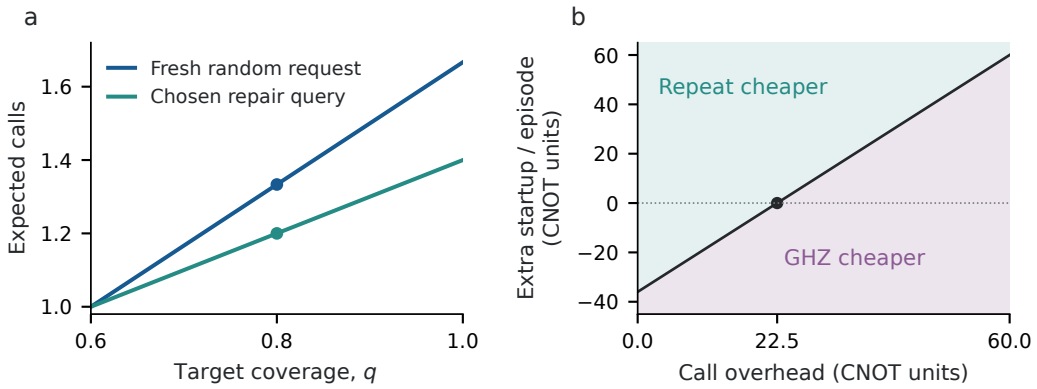

Figure 4: (a) Fresh random requests and chosen repair queries have different call costs. Points reproduce Bell coverage $q = .8$ from a product probe. (b) Cost comparison at 80% power and 5% false alarms for known $(e_0, e_1) = (.02, .164)$. GHZ uses 18 calls and 111.6 logical CNOTs; a product-initialized repeated-query policy uses 19.6 expected calls and 75.6 CNOTs. The boundary includes extra GHZ startup cost per episode. These are two attaining policies, not the full adaptive frontier.

At equal operating performance, entanglement reduces lifetime cost exactly when its extra startup cost is smaller than the accumulated saving in preparation and detection (Eq. (19)). Previous IBM diagnosis runs measured GHZ power gains of 9.11 and 16.34 points over a selected product probe, with frozen aggregate alarm rules and dynamic coherence controls. Their different calibrations prevent a matched-cost hardware comparison with the adaptive policy (Appendix O).

Classical transaction co-location. A database also chooses which records to place together before requests arrive. A transaction footprint F_t succeeds when all its records share a shard, subject to a capacity cap and no replication. Schism formulates this hypergraph objective and uses tuple coaccess graphs as a surrogate (Curino et al., 2010). On structured schemas, we recover the same allocation problem.

Theorem 2 transfers exactly to row/column transactions on r disjoint $s \times s$ tables when capacity is $C = (s-1)k + 1$ and $s \geq \max\{2, k, \lfloor (k-1)^2/4 \rfloor + 2\}$. Allowing rs shards, the minimax locality regret is $\Theta(\min\{1, \sqrt{rk/m}\})$ (Corollary 2). Larger tables need not require more requests, although transaction width and storage resources grow. All 15,360 checks of actual record placements reproduce the predicted masks.

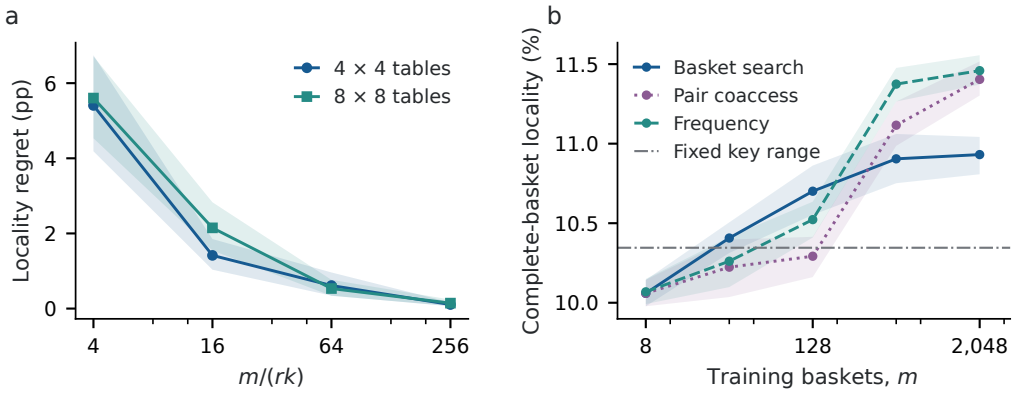

Figure 5: (a) Exact empirical co-location on structured tables, with requests scaled by rk. Curves average $r \in \{1, 4\}$ and $k \in \{1, 2, 3\}$, with 32 instances per cell; bands bootstrap training instances. (b) Complete-basket locality on the public Online Retail trace, with 3,922 records and eight shards of capacity 512. Learned methods share a training prefix; fixed key range uses none. Bands bootstrap 16 request streams conditional on the fixed catalogue and test trace. All three capacities and the exact small-schema study appear in Appendix M.

On public purchase baskets (Chen, 2015), we test both exact optimization on 12/24-item projections and a heuristic on the full 3,922-record catalogue. The full study scores all 3,992 held-out invoices without projection. At capacity 512 and 512 training baskets, locality is 10.90% for basket-based search, 11.37% for same-budget frequency grouping, and 10.35% for fixed key-range placement. The simpler frequency control wins this comparison. Uniform SmallBank footprints leave no allocation to learn: all balanced placements have the same locality.

8 Related work and implications

Exact separable stabilizer polytopes and attaining product states are known for selected GHZ and cluster families (Jafarizadeh et al., 2008). Zander & Becker (2025, Propositions A.3–A.4) give our linear cut inequalities. Knips et al. (2016) optimize weighted independent sets of cut-anticommutativity graphs for squared correlations; Li et al. (2026) derive linear graph-generator bounds using crossing-edge matchings. Our constructive region for independent CSS families under arbitrary partition mixtures yields sharp learning laws. Stable-set integrality (Chvátal, 1975) and component-order connectivity (Drange et al., 2016) are classical ingredients.

Predictive $\mathcal{V}$-information and the Decodable Information Bottleneck describe predictor-dependent information (Xu et al., 2020; Dubois et al., 2020); our logarithmic-loss extension applies this prediction viewpoint with physically restricted observations and unrestricted classical decoders. Data hiding and locally indistinguishable product ensembles separate storage from access (Terhal et al., 2001; Bennett et al., 1999). Roll (2026) studies quantum language memory through gate ablations and density-matrix interventions; we study allocation's request complexity. Channel discrimination benefits from entanglement (Piani & Watrous, 2009). Here we identify the optimal experiment for a fixed query menu and transfer its allocation-learning cost.

Memory size alone does not determine the cost of learning an allocation. Paths create more choices as they grow; biclique regions need not. The same distinction arises in classical co-location. Practical gains also depend on preparation costs and the workload, which can favor simpler choices. We have yet to characterize general measurements or test the learning laws across independent hardware jobs.

REPRODUCIBILITY STATEMENT

The supplement provides raw observations, seeds, encoders, resource counts and replay code. The appendix contains all main proofs and the protocols for the current experiments. A small installable package reproduces the path optimizer and online sampler. The revision97 entry point checks the new hardware, classical and interface evidence, figures and compiled manuscript; historical numerical checks retain their version-specific commands. The extended evidence record preserves auxiliary results and earlier device acquisitions.

AI USE STATEMENT

Generative AI assisted with theoretical models and mathematical claims, proof development and writing, hypothesis refinement, experimental design, method implementation, synthetic-data generation, data processing, result interpretation, and figure preparation. It also assisted with literature review and manuscript drafting and editing. The authors take responsibility for the final manuscript and artifacts.

ETHICS STATEMENT

The experiments use synthetic tasks, measurements from a quantum processor, and a public purchase dataset. The transaction study reads stock codes, invoice identifiers, times, quantities and prices; it does not read customer identifiers or link purchases to people. It reports aggregate locality only. The hardware results compare fixed implementations. Their interpretation is limited to the stated measurement and control assumptions and does not establish a general quantum learning speedup.

REFERENCES

Peter L. Bartlett and Shahar Mendelson. Rademacher and Gaussian complexities: Risk bounds and structural results. *Journal of Machine Learning Research*, 3:463–482, 2002. URL https://jmlr.org/papers/v3/bartlett02a.html.

BenchBase contributors. BenchBase: SmallBank workload implementation. Software repository, 2025. URL https://github.com/cmu-db/benchbase/tree/33c00473807ebd49304d114a6d769d2d2b2bbb34. Commit 33c00473807e; accessed September 8, 2026.

Charles H. Bennett, David P. DiVincenzo, Christopher A. Fuchs, Tal Mor, Eric Rains, Peter W. Shor, John A. Smolin, and William K. Wootters. Quantum nonlocality without entanglement. *Physical Review A*, 59(2):1070–1091, 1999. doi: 10.1103/PhysRevA.59.1070. URL https://arxiv.org/abs/quant-ph/9804053.

Daqing Chen. Online Retail. UCI Machine Learning Repository, 2015. URL https://doi.org/10.24432/C5BW33. Dataset.

V. Chvátal. On certain polytopes associated with graphs. *Journal of Combinatorial Theory, Series B*, 18(2):138–154, 1975. doi: 10.1016/0095-8956(75)90041-6.

Carlo Curino, Evan Jones, Yang Zhang, and Sam Madden. Schism: a workload-driven approach to database replication and partitioning. *Proceedings of the VLDB Endowment*, 3(1–2):48–57, 2010. doi: 10.14778/1920841.1920853. URL https://www.vldb.org/pvldb/vol3/R04.pdf.

Djellel Eddine Difallah, Andrew Pavlo, Carlo Curino, and Philippe Cudré-Mauroux. OLTP-Bench: An extensible testbed for benchmarking relational databases. *Proceedings of the VLDB Endowment*, 7(4):277–288, 2013. doi: 10.14778/2732240.2732246. URL https://www.vldb.org/pvldb/vol7/p277-difallah.pdf.

Pål Grønås Drange, Markus Dregi, and Pim van 't Hof. On the computational complexity of vertex integrity and component order connectivity. *Algorithmica*, 76(4):1181–1202, 2016. doi: 10.1007/s00453-016-0127-x. URL https://arxiv.org/abs/1403.6331.

Yann Dubois, Douwe Kiela, David J. Schwab, and Ramakrishna Vedantam. Learning optimal representations with the decodable information bottleneck. In *Advances in Neural Information Processing Systems*, volume 33, pp. 18674–18690. Curran Associates, Inc., 2020. URL https://papers.nips.cc/paper/2020/hash/d8ea5f53c1b1eb087ac2e356253395d8-Abstract.html.

David Haussler. Sphere packing numbers for subsets of the Boolean n-cube with bounded Vapnik–Chervonenkis dimension. *Journal of Combinatorial Theory, Series A*, 69(2):217–232, 1995. doi: 10.1016/0097-3165(95)90052-7.

Teiko Heinosaari and Takayuki Miyadera. Qualitative noise-disturbance relation for quantum measurements. *Physical Review A*, 88(4):042117, 2013. doi: 10.1103/PhysRevA.88.042117. URL https://doi.org/10.1103/PhysRevA.88.042117.

M. A. Jafarizadeh, G. Najarbashi, Y. Akbari, and H. Habibian. Multi-qubit stabilizer and cluster entanglement witnesses. *The European Physical Journal D*, 47(2):233–255, 2008. doi: 10.1140/epjd/e2008-00028-0. URL https://arxiv.org/abs/0704.2414v2.

Lukas Knips, Christian Schwemmer, Nico Klein, Marcin Wieśniak, and Harald Weinfurter. Multipartite entanglement detection with minimal effort. *Physical Review Letters*, 117(21):210504, 2016. doi: 10.1103/PhysRevLett.117.210504. URL https://journals.aps.org/prl/abstract/10.1103/PhysRevLett.117.210504.

Dennis Kretschmann, Dirk Schlingemann, and Reinhard F. Werner. The information-disturbance tradeoff and the continuity of Stinespring's representation. *IEEE Transactions on Information Theory*, 54(4):1708–1717, 2008. doi: 10.1109/TIT.2008.917696. URL https://doi.org/10.1109/TIT.2008.917696.

Joon Kwon and Vianney Perchet. Gains and losses are fundamentally different in regret minimization: The sparse case. *Journal of Machine Learning Research*, 17(227):1–32, 2016. URL https://jmlr.org/papers/v17/15-503.html.

Nicky Kai Hong Li, Xi Dai, Manuel H. Muñoz-Arias, Kevin Reuer, Marcus Huber, and Nicolai Friis. Detecting genuine multipartite entanglement in multi-qubit devices with restricted measurements. *Nature Communications*, 17(1):1707, 2026. doi: 10.1038/s41467-026-69320-4. URL https://www.nature.com/articles/s41467-026-69320-4.

Georgios S. Paschos, Apostolos Destounis, Luigi Vigneri, and George Iosifidis. Learning to cache with no regrets. In *IEEE INFOCOM 2019 - IEEE Conference on Computer Communications*, pp. 235–243. IEEE, 2019. doi: 10.1109/INFOCOM.2019.8737446. URL https://arxiv.org/abs/1904.09849.

Marco Piani and John Watrous. All entangled states are useful for channel discrimination. *Physical Review Letters*, 102(25):250501, 2009. doi: 10.1103/PhysRevLett.102.250501.

D. Ristè, M. Dukalski, C. A. Watson, G. de Lange, M. J. Tiggelman, Ya. M. Blanter, K. W. Lehnert, R. N. Schouten, and L. DiCarlo. Deterministic entanglement of superconducting qubits by parity measurement and feedback. *Nature*, 502(7471):350–354, 2013. doi: 10.1038/nature12513. URL https://doi.org/10.1038/nature12513.

Nathan Roll. Entanglement as memory: Mechanistic interpretability of quantum language models, 2026. URL https://arxiv.org/abs/2603.26494.

Barbara M. Terhal, David P. DiVincenzo, and Debbie W. Leung. Hiding bits in Bell states. *Physical Review Letters*, 86(25):5807–5810, 2001. doi: 10.1103/PhysRevLett.86.5807. URL https://arxiv.org/abs/quant-ph/0011042.

Frederik vom Ende. Progress on the Kretschmann–Schlingemann–Werner conjecture. *Quantum Information and Computation*, 23(15–16):1319–1330, 2023. doi: 10.26421/QIC23.15-16-5. URL https://doi.org/10.26421/QIC23.15-16-5.

Yilun Xu, Shengjia Zhao, Jiaming Song, Russell Stewart, and Stefano Ermon. A theory of usable information under computational constraints. In *International Conference on Learning Representations*, 2020. URL https://openreview.net/forum?id=r1eBeyHFDH.

Bin Yu. Assouad, Fano, and Le Cam. In David Pollard, Erik Torgersen, and Grace L. Yang (eds.), *Festschrift for Lucien Le Cam*, pp. 423–435. Springer, 1997. doi: 10.1007/978-1-4612-1880-7_29.

René Zander and Colin Kai-Uwe Becker. Benchmarking multipartite entanglement generation with graph states. *Advanced Quantum Technologies*, 8(1):2400239, 2025. doi: 10.1002/qute.202400239. URL https://advanced.onlinelibrary.wiley.com/doi/10.1002/qute.202400239.

Appendix guide. The appendix gives the contrast-region proof, the sharp learning laws, experimental protocols, interface conversion and classical transfer. The extended evidence supplement retains auxiliary logarithmic-loss, online, bounded-degree and historical hardware analyses in full.

A Detector preservation and permitted reports

The instrument acts on the complete retained memory, with no additional input correlated with G. The decoder observes only its classical report and the query. The contract concerns all input density operators, including states absent from the particular bit code. Preserving just the actual codewords would not exclude local decoding of a product repetition code.

A.1 Exact compatibility

Let $\{\mathcal{J}_y\}$ be CP instrument outcomes with $\sum_y \mathcal{J}_y = \mathcal{L}_P$. For Choi matrices, $0 \preceq C(\mathcal{J}_y) \preceq C(\mathcal{L}_P)$. The latter has support $\operatorname{span}\{|\Pi_+\rangle\!\rangle, |\Pi_-\rangle\!\rangle\}$. Every Kraus operator of every outcome therefore has the form $A_{yj} = a_{yj}\Pi_+ + b_{yj}\Pi_-$. Orthogonality of the projectors gives

$$E_y = \sum_j A_{yj}^\dagger A_{yj} = q(y|+)\Pi_+ + q(y|-)\Pi_-, \qquad q(y|+) = \sum_j |a_{yj}|^2, \quad q(y|-) = \sum_j |b_{yj}|^2.$$

The effects sum to I, so q is stochastic. Conversely, measuring the sharp parity and applying q realizes each such report. This proves the stated equality of report classes. It is a special case of channel–observable compatibility (Heinosaari & Miyadera, 2013). The contract is stronger than preserving the value of P: a refinement inside an eigenspace can commute with P while destroying its coherence. Native parity meters motivate the preservation requirement (Ristè et al., 2013); we do not infer this requirement from classical storage.

A.2 A conservative approximate bound

Suppose the actual nonselective channel $\mathcal{E}_t$ obeys $\|\mathcal{E}_t - \mathcal{L}_{P_t}\|_\diamond \le \delta_t$, with the full diamond norm, not half that norm. Pad the Stinespring environments to a common dimension at least the sum of their Kraus ranks. The continuity theorem (Kretschmann et al., 2008), in the form of vom Ende (2023, Proposition 1), provides an alignment with isometry distance at most $\sqrt{\delta_t}$. Padding is material: the same optimal bound need not hold in an arbitrarily prescribed minimal environment (vom Ende, 2023, Example 1).

An instrument's classical report is a POVM on the channel environment. Extend that POVM to the padded space. The actual report channel $\mathcal{C}_t$ is then within $2\sqrt{\delta_t}$ in diamond norm of some parity-postprocessing channel $\mathcal{C}_t^0$. For $\Delta = D(\tau_0 - \tau_1)$, $\|\Delta\|_1 \le 2D$, while binary risk is

$$R_{\mathcal{C}} = \frac{1}{2} - \frac{1}{4}\sum_t \pi_t \|\mathcal{C}_t(\Delta)\|_1.$$

The triangle inequality gives, uniformly over all allowed encoders,

$$R_{\mathcal{F}}^{\mathrm{relaxed}} \ge \max\left\{h,\ R_{\mathcal{F}}^{\mathrm{sharp}} - D\sum_t \pi_t\sqrt{\delta_t}\right\}. \tag{9}$$

The reference is the ideal *sharp-parity* optimum. The nonselective channel contract does not enforce a chosen reporting visibility. It also does not guarantee a useful actual report: the one-outcome instrument $\mathcal{J}_* = \mathcal{L}_P$ has $\delta = 0$ and risk $1/2$ for every encoder. A device comparison requires an informative predictor below the comparator bound, in addition to channel calibration.

For the disjoint three-vertex path gadget family (proved in the extended supplement), sharp separable risk is $h + D/4$, and the depth-two oracle attains $h + D(1-\theta)/8$. If all $\delta_t \le \delta$, the latter beats the relaxed separable class by at least $D[(1+\theta)/8 - \sqrt{\delta}]$. The sufficient radius $\delta < 1/64$ is independent of the number of gadgets.

The all-input condition rules out storing the classical bit in an unmeasured register and replacing the supplied detector by a local selector. The extended evidence supplement gives explicit disturbances and the full resource table for those altered interfaces.

B PROOF OF THE EXACT CONTRAST REGION

Assume $q \geq 1$, independent commuting Hermitian CSS Pauli generators and a nonempty allowed partition family. We use the conventional uniform prior and binary prediction loss throughout this region theorem.

B.1 SINGLE-STATE BOUNDS AND DOWNWARD CLOSURE

Independence makes the symplectic constraints for a tensor-product Pauli Q with $QP_tQ^\dagger = -P_t$ solvable. It preserves every partition class. For any allowed pair, $\rho = (\tau_0 + Q\tau_1 Q^\dagger)/2$ has $|\operatorname{Tr}(P_t\rho)| = |\operatorname{Tr}[P_t(\tau_0 - \tau_1)]|/2$. Conversely, $(\rho, Q\rho Q^\dagger)$ realizes the absolute correlations of ρ. This gives the single-state reduction used in the main text.

For a state product across Π, let $x_t = |\operatorname{Tr}(P_t\rho)|$. If u, v are adjacent in H_Π, global commutation implies an even, nonzero number of blocks with local anticommutation. Choose two, A, B, and denote their expectation pairs by (a_u, a_v) and (b_u, b_v). Anticommutation gives $a_u^2 + a_v^2 \leq 1$ and $b_u^2 + b_v^2 \leq 1$. The remaining factors have absolute value at most one, so

$$x_u + x_v \leq |a_u b_u| + |a_v b_v| \leq 1.$$

Together with $0 \leq x_t \leq 1$, these are the stable-set inequalities for a bipartite graph (Chvátal, 1975). Thus $x \in \mathrm{STAB}(H_\Pi)$.

Let $\mathcal{P} = \operatorname{conv} \bigcup_\Pi \mathrm{STAB}(H_\Pi)$. It is downward closed. Constructively, represent $z \in \mathcal{P}$ by a distribution of feasible independent sets. For $0 \leq c \leq z$, retain coordinate t independently with probability c_t/z_t, and omit it when $z_t = 0$. The resulting subset stays feasible and has expected indicator c. For a mixture of block-product states, its absolute expectation vector is below the average of their absolute vectors, so also lies in $\mathcal{P}$. The contrast vector of any two allowed codewords is below the mean of their absolute vectors. This proves $c \in \mathcal{P}$, including codewords whose partitions and mixtures differ.

B.2 ATTAINMENT

For an independent set I of H_Π, define τ_g^I by Eq. (4). Global commutation makes it positive. Independence means every nonidentity product is traceless, so its trace is one. It has expectation $(-1)^g$ for selected generators and zero for every unselected generator.

Restrictions of selected generators commute inside every block. A simultaneous eigenbasis on each block supplies a product basis in which τ_g^I is diagonal and nonnegative. The state is therefore separable across Π. For nonempty I, the two codewords occupy opposite eigenspaces of any selected generator and have orthogonal supports. For $I = \varnothing$, set both codewords to $I/2^d$.

For weights λ_I, the pair $\tau_g = \sum_I \lambda_I \tau_g^I$ has $\operatorname{Tr}(P_t\tau_g) = (-1)^g \sum_{I \ni t} \lambda_I$. It realizes every point of $\mathcal{P}$ exactly, completing Theorem 1. Maximizing a nonnegative linear workload functional selects a nonempty indicator (also when all weights vanish), so an information-preserving optimum always exists.

The equality concerns binary prediction-risk vectors, not equivalence of full statistical experiments. For example, equal mixtures of the XX and ZZ projector codes give $\operatorname{Tr}(\tau_0\tau_1) = 1/8$, despite each selected pair being orthogonal. Randomly choosing a model after training and recording that choice is distinct from an unobserved mixture on every trial.

Mixtures of attaining pairs need not preserve the bit, although every nonzero vertex does. The linear-risk optimum can always choose such a vertex. A worked lossless mixture is given in the extended supplement.

B.3 A SUFFICIENT CONDITION BEYOND CSS

The same region theorem holds for independent commuting Pauli generators if every allowed partition satisfies: (i) H_Π is perfect; and (ii) for every maximal clique with at least two vertices, there are two blocks on each of which the clique's restrictions pairwise anticommute. For such a clique J, anticommutation gives $\sum_{t \in J} a_t^2, \sum_{t \in J} b_t^2 \leq 1$, hence $\sum_{t \in J} x_t \leq \sum |a_t b_t| \leq 1$. Include singleton

inequalities $x_t \le 1$. Perfection makes these clique constraints describe $\mathrm{STAB}(H_\Pi)$ (Chvátal, 1975). The preceding attainment and mixture arguments are unchanged. For two-block partitions, global commutation makes condition (ii) automatic. This is a sufficient condition, not a characterization of every family admitting an exact combinatorial rule.

The independent fixed query menu $\{XXI, YYZ, ZZI\}$ satisfies both conditions for every partition. Its conflict graph is K_3 when the first two qubits are in different blocks, with anticommutation shared by those blocks, and is empty otherwise.

Three failures delimit the result, all with $h = 0$ and sharp reports. For dependent queries $\{ZI, IZ, ZZ\}$, the conflict graph is empty, but the equally weighted optimal error is $1/6$, not zero: two joint eigenvalue strings can differ in at most two positions. For $\{XZZ, ZXZ, ZZX\}$ on singleton blocks, the conflict graph is perfect (K_3), but no common two blocks support its clique. The orthogonal product pair with antipodal local Bloch vectors $\pm(1/\sqrt{3}, 0, \sqrt{2/3})$ has risk $1/2 - 1/(3\sqrt{3}) = 0.30754991$, below the independent-set formula's $1/3$. Finally, mixtures of lossless code pairs need not be lossless, as the XX/ZZ example in the extended supplement shows.

B.4 Graph components and depth

For graph-state generators on a bipartite graph, local Clifford conjugation preserves all commutation relations. Two generator restrictions conflict across a partition exactly when their graph edge crosses the partition. A minimum-weight vertex cover of the crossing edges leaves every surviving connected component inside one block. Conversely, delete any vertex set whose remaining components have size at most k, group those components, and make deleted vertices singletons. Every crossing edge is covered. Therefore, over all depth-k partitions,

$$R_k^* = \frac{1}{2} - \frac{D}{2}\left[\sum_i a_i - \min_{\substack{U \subseteq V \\ \max_{B \in \mathrm{cc}(G-U)} |B| \le k}} \sum_{i \in U} a_i\right].$$

Extra hardware constraints on partitions can invalidate the converse construction and must be imposed separately. Deleted vertices remove query requirements, not qubits.

Prepare each retained graph component in its graph state, with deleted sites in $|0\rangle$, then apply Z^g to each retained vertex. Retained generator expectations are $(-1)^g$; a deleted generator has zero expectation because it contains X on a deleted site. This pure block code attains the displayed optimum. For a path, each disjoint group of $k+1$ consecutive vertices requires a deletion, giving $\lfloor d/(k+1) \rfloor$ deletions under uniform weights. Deleting every $(k+1)$st vertex attains the bound. For $D > 0$ and sharp reports, attaining risk h requires every active connected component to fit within a block.

C Learning bounds for physical encoders

For a fixed measurement family and depth cap k, write

$$\mathfrak{M}_m(\Gamma, k) = \inf_{\widehat{\tau}} \sup_{\pi \in \Delta_{q-1}} \mathbb{E}_{T_{1:m} \sim \pi^m, \widehat{\tau}}[R_\pi(\widehat{\tau}) - R^*_{\pi,k}].$$

The infimum includes randomized maps from m query identities to any allowed mixed codeword pair, with its optimal classical decoder. The learner knows the source reliability, measurement family, reporting parameters and partition constraints. The query distribution is unknown. Block placement is unrestricted except for the stated partition family; lower bounds use sharp reports.

C.1 Finite-class upper bound

Let $\mathcal{A}$ be the feasible independent-set indicators and $N = |\mathcal{A}| \le 2^q$. The score of an indicator on query t is $v_t \mathbf{1}\{t \in I\} \in [0,1]$. With probability at least $1-\delta$, every score average differs from its expectation by at most $\sqrt{\log(2N/\delta)/(2m)}$. Two deviations and the factor $D/2$ in the risk give

$$R(\widehat{I}) - \min_{\tau_0, \tau_1 \in \mathcal{S}_\mathcal{F}} R \le D\sqrt{\frac{\log(2N/\delta)}{2m}}, \tag{10}$$

capped by $D/2$. The expected version replaces δ by the standard finite-class maximal-deviation bound and has $D\sqrt{\log(2N)/(2m)}$. Theorem 1 makes this a comparison with every allowed mixed physical encoder. The learner receives only the stipulated query samples and known interface parameters. These are standard concentration arguments; exact risk completeness supplies their physical comparator.

C.2 Allocation geometry changes the learning rate

Let the measurement graph be the complete bipartite graph $K_{a,b}$, with color classes A, B, $q = a + b$ qubits and $1 \le k \le \min(a, b)$. Allow every partition of depth at most k. A retained query set meeting both colors induces one connected component, so it fits a block exactly when its size is at most k. Every one-color set is feasible. The exact contrast region is therefore the convex hull of these indicators.

For nonnegative weights $w_i = \pi_i v_i$, the optimum score is

$$V_k(w) = \max\left\{\sum_{i\in A} w_i,\ \sum_{i\in B} w_i,\ \mathrm{Top}_k(w)\right\}, \tag{11}$$

where Top_k sums the k largest coordinates. A monochromatic top-k set is dominated by its full color class. Evaluating the three candidates costs $O(q\log(k+1))$ with a heap, or $O(q)$ with linear-time selection. This is an elementary optimizer for the stated complete physical encoder class, not a quantum speedup.

Only undominated allocations need to be learned. The maximal feasible sets are

$$\mathcal{M}_k = \{A, B\} \cup \{S : |S| = k,\ S \cap A \neq \varnothing,\ S \cap B \neq \varnothing\}.$$

Their indicator class has VC dimension exactly k. A set of k vertices inside A is shattered: A and B give the full and empty traces; complete each nonempty proper subset to a mixed k-set using vertices in B. No $(k+1)$-set is shattered. If it meets both colors, its all-positive trace is unavailable. If it is monochromatic, a trace with exactly k positives is unavailable: a mixed k-set has at most $k-1$ vertices of that color, whereas the full color includes all $k+1$. This also covers $k = 1$, when the frontier is simply $\{A, B\}$.

The full downward-closed feasible class has VC dimension $\max(a, b)$, since every subset of a color is feasible, while a larger set necessarily crosses the colors and cannot be included. Thus counting all feasible indicators, including dominated ones, can overstate the statistical difficulty by an arbitrarily large factor.

The deviation bound and risk conversion. For a set class $\mathcal{M}$ of VC dimension $V \ge 1$ and fixed $v_t \in [0, 1]$, put $f_I(t) = v_t \mathbf{1}_I(t)$. The standard expected VC bound is

$$\mathbb{E}\sup_{I\in\mathcal{M}} |(\widehat{\pi} - \pi) f_I| \le C_0 \min\{1, \sqrt{V/m}\}$$

for a universal constant C_0. For $v = 1$, this follows by symmetrization from the Gaussian VC bound of Bartlett & Mendelson (2002, Theorem 6 and Lemma 4), using the entropy bound of Haussler (1995). Known visibility cannot increase empirical L_2 distances: $\|v(\mathbf{1}_I - \mathbf{1}_J)\|_{L_2(\widehat{\pi})} \le \|\mathbf{1}_I - \mathbf{1}_J\|_{L_2(\widehat{\pi})}$. The same covering-number argument therefore applies. If I^* maximizes the population score and $\widehat{I}$ maximizes the empirical score, then

$$R_\pi(\widehat{I}) - R_\pi(I^*) = \frac{D}{2}\pi(f_{I^*} - f_{\widehat{I}}) \le D \sup_{I\in\mathcal{M}} |(\widehat{\pi} - \pi) f_I|.$$

Taking expectations and setting $V = k$ gives the claimed rate. Nonnegative weights make maximal sets sufficient; exact region completeness supplies the full physical comparator.

Capacity-controlled learning from request identities is also familiar in classical caching. For fractional caching with unit hit utilities and capacity $C < N/2$ in an N-file catalogue, Paschos et al. (2019, Theorem 2) give cumulative regret at most $\sqrt{2CT}$ against the best fixed cache, independent of N. Here the objective is batch excess risk, and the physical region determines a top-k/color-class frontier and a lower bound over arbitrary mixed encoders.

A matching lower bound over physical learners. Set $v_i = 1$. Choose k active vertices in each color and pair them. For unknown signs σ_j and $0 \le \theta \le 1/2$, assign

$$\pi_{j,A} = \frac{1+\sigma_j\theta}{2k}, \qquad \pi_{j,B} = \frac{1-\sigma_j\theta}{2k},$$

with zero probability on all other queries. Projection of the exact region onto these $2k$ coordinates is $\{c \in [0,1]^{2k} : \sum_i c_i \le k\}$. Every physical learner can therefore be replaced, without knowing the signs, by a randomized subset of at most k active coordinates. Fill it to size k. The number of doubly selected pairs then equals the number of omitted pairs. Replace each such double and omission by one uniformly selected endpoint in each pair. Every pair has total mass $1/k$, so this transformation preserves expected captured mass for every sign vector, conditionally on the original subset. It need not preserve risks outside this hard family.

A wrong endpoint choice incurs excess $D\theta/(2k)$. Neighboring signs have one-sample KL divergence

$$\frac{\theta}{k}\log\frac{1+\theta}{1-\theta} \le \frac{4\theta^2}{k}.$$

For $\theta = \min\{1/2, \frac{1}{4}\sqrt{k/m}\}$, their m-sample total variation is at most $\sqrt{2}/4 < 1/2$. The coordinate testing error is at least $1/4$, giving

$$\inf_{\widehat{\tau}} \sup_{\pi} \mathbb{E}[R(\widehat{\tau}) - R^*_{\pi,k}] \ge \frac{D}{32}\min\{1, \sqrt{k/m}\}. \tag{12}$$

The upper and lower bounds establish the sharp rate. They allow arbitrary workload distributions, including zeros, and unrestricted block placement subject to the depth cap.

C.3 Connected regions and the effective allocation dimension

The local and complete-bipartite laws extend to a connected family between those extremes. Partition the vertices of a bipartite graph Γ into r regions $M_j = A_j \cup B_j$, each inducing a complete bipartite graph. A designated set $P_j \subset M_j$ contains its connection vertices: every edge between regions has both endpoints in these sets. Assume $|P_j| \le p$ and that each of $A_j \setminus P_j$ and $B_j \setminus P_j$ contains at least k vertices. The connections between regions can be arbitrary, provided Γ remains bipartite. The word region denotes this chosen vertex partition; the physical encoder may use blocks crossing its boundaries.

For sharp graph-generator reports, $m \ge 1$ request observations, and all physical encoders of depth at most k,

$$\frac{D}{32}\min\{1, \sqrt{rk/m}\} \le \mathfrak{M}_m(\Gamma, k) \le CD\min\left\{1, \sqrt{\frac{rk + \sum_j |P_j|}{m}}\right\}, \tag{13}$$

where C is universal. For fixed p, this is $\Theta_p(D\min\{1, \sqrt{rk/m}\})$, with constants independent of the region sizes, r and k. Both r and k may grow. The upper bound is attained by exact empirical maximization over maximal feasible query sets; every output has a lossless code. The lower bound permits arbitrary randomized mixed physical encoders and grants their optimal decoder.

The maximal class has dimension at most $rk + \sum_j |P_j|$. The exact physical region is the convex hull of indicators S whose selected connected components have size at most k. Consider an inclusion-maximal feasible S. If it meets both colors of region j, its selected region vertices lie in one component, so there are at most k of them. If it meets only one color, every nonconnection vertex of that color must be selected: a missing one would have no selected neighbor and could be added as a singleton. Edges between connection vertices do not change this argument.

No $k+1$ nonconnection vertices in one region can be shattered by the maximal class. A test set meeting both colors lacks the all-positive trace, which would require a component larger than k. A monochromatic test set lacks a trace with exactly k positives: a monochromatic selection includes the entire test set, while a mixed selection containing those k positives also needs an opposite-color vertex. Its component would again exceed k. The projected maximal class on each region interior therefore has VC dimension at most k. A globally shattered set has at most k interior vertices per region and at most $\sum_j |P_j|$ connection vertices. The VC bound and the risk conversion in Appendix C.2 prove the upper inequality.

Connections do not remove the capacity lower bound. Choose k nonconnection vertices from each color of each region. Projection onto these $2rk$ active coordinates is exactly

$$\prod_{j=1}^{r} \left\{ c^{(j)} \in [0,1]^{2k} : \sum_{i} c_i^{(j)} \le k \right\}.$$

Every feasible indicator satisfies each capacity inequality. A monochromatic trace has only k active vertices available, while a mixed trace lies in one component of size at most k. Conversely, select any at-most-k active vertices per region and no others. No selected interregion edge remains, and each component fits the cap. Convexification gives the product of the uniform-matroid independence polytopes. This proof uses the complete physical region; partitions crossing regions cannot enlarge the projection.

Pair the active colors within each region and assign

$$\pi_{j,\ell,A} = \frac{1+\sigma_{j\ell}\theta}{2rk}, \qquad \pi_{j,\ell,B} = \frac{1-\sigma_{j\ell}\theta}{2rk}, \quad \sigma_{j\ell} \in \{-1,1\}, \quad 0 \le \theta \le \tfrac{1}{2}.$$

All other queries have zero probability. Decompose any physical learner's projected contrast into product subset indicators and fill each region to size k. Within each region, pair each doubly selected pair with an omitted pair and replace them by uniform single-endpoint choices. Every pair has total mass $1/(rk)$, so this replacement preserves expected captured mass for every sign vector. Filling can only improve it. The resulting learner chooses one endpoint in each of rk pairs without knowing the signs.

A wrong choice costs $D\theta/(2rk)$ in excess risk. Neighboring signs have one-sample divergence at most $4\theta^2/(rk)$. Choosing $\theta = \min\{1/2, \frac{1}{4}\sqrt{rk/m}\}$ bounds sample total variation by $\sqrt{2}/4 < 1/2$ in both branches. The average testing error is at least $1/4$ per pair, giving $D\theta/8 \ge (D/32)\min\{1, \sqrt{rk/m}\}$. The oracle chooses the more frequent endpoint in every pair and has risk $h + D(1-\theta)/4$. This argument also covers $k = 1$.

A positive-weight allocation across regions. Take two $K_{3,3}$ regions with colors A_1, B_1, A_2, B_2 and a single edge from $b \in B_1$ to $a \in A_2$. The weights on B_1 and A_2 are $(6,5,5)$, with six at b, a; all six other weights are one. Normalize by the total 38. At depth two, retaining both preferred colors supports weight 32. Only a, b share a component; the four other retained vertices are singletons. Any mixed selection within a region contains at most two vertices and has weight at most seven, while the less-favored full color has weight three. Thus 32 is the unique optimal retained-query weight pattern. At depth one, one must also discard a or b, reducing the best weight to 26. Switching a whole region to its other color is worse. The exact region therefore gives optimal errors $3/38$ and $3/19$, respectively, over the full physical classes. Its projector codes retain the same bit. Independent enumeration of all 2^{12} query subsets at both caps reproduces these values.

Why the connection bound matters. Join two $K_{s+1,s+1}$ regions by a matching between s vertices of B_1 and s vertices of A_2. Each facing color still has one nonconnection vertex. At depth one, projection onto the $2s$ matching endpoints is exactly a product of s two-element rank-one capacities: one cannot select both endpoints of an edge, and every other selection is feasible by omitting all nonmatching vertices. The paired-testing argument above now gives $\Omega(D\min\{1, \sqrt{s/m}\})$; the finite-class upper bound on $4(s+1)$ vertices matches it. Thus fixed $r = 2$ and $k = 1$ do not give a size-independent rate when the connection count grows. The same independent source exhaustively checks the projection for $s = 1, 2, 3$; the argument establishes it for every s. This boundary is an application of the capacity lower bound.

An exact optimizer for a chain of regions. Consider a chain of $K_{s,s}$ regions, each with a left connection vertex in A and a right one in B. Consecutive right and left vertices are joined. For $s \ge k+1$, Eq. (13) gives the sharp rate $\Theta(D\min\{1, \sqrt{rk/m}\})$ on $d = 2rs$ qubits. Increasing s need not increase this statistical cost; increasing r does. At fixed s, k, the rate is dimensional, consistent with the bounded-degree law. Larger s also increases query support, so this comparison does not fix detector cost.

The empirical optimum can be computed without enumerating all allocations. Process regions from left to right, with state $t \in \{0, \dots, k\}$ equal to the size of the selected component touching the

preceding right connection vertex; $t = 0$ means that vertex is absent. A mixed-color option with n selected vertices and left/right selection bits L, R forms one local component. Set $z = n + Lt$, reject $z > k$, and send state Rz to the next region. If $L = 0$, the incoming component closes.

For an A-only option, include all nonconnection A vertices and optionally its left connection vertex. Those interior vertices are separate singletons. Selecting the left vertex joins only one vertex to the incoming component, so require $t + 1 \le k$; the outgoing state is zero. A B-only option similarly includes its interior singletons and has outgoing state zero or one, according to whether the right vertex is selected. Empty options can be included for boundary cases with no interior vertices.

Sort the interior weights in each color. For every mixed size and connection pattern, prefix sums give the best split between colors. There are $O(k^2)$ candidate splits but only $O(k)$ resulting options; $O(k)$ incoming states give $O(rk^2)$ scalar work across the chain, after $O(d \log d)$ sorting. This is a sufficient boundary state, so induction proves the recurrence exact. Equal objectives prefer greater selected cardinality, ensuring a maximal optimum; a fixed mask order resolves remaining ties. Integer-mask costs are additional. The implementation uses floating-point comparisons and does not certify exact ordering of nearly equal real objectives.

Independent checks. The released chain optimizer passes 1,300 exhaustive weighted objectives on 22 graphs, including 1,000 exact integer-weight cardinality and maximality checks. A separate implementation checks 336 connected port graphs, 9,496 capped physical partitions of a ten-qubit example, and 20,109 weighted optimizations. It compares the released optimizer against 44,938 exhaustive graph-oracle workloads, including zero weights, asymmetric regions, empty interiors and $k = 1$. These finite checks support the derivations above; they do not establish the asymptotic claims. Both implementations and their complete results are in the reproducibility archive.

D Preparation noise, algorithms and preserved information

D.1 Exact circuit-family objective

For a fixed selected set S, prepare graph-state runs, put deleted sites in $|0\rangle$, and apply Z^g to every selected site. A ZZ error after a retained edge flips precisely its two incident generator expectations. Independent errors therefore give Eq. (8). An unselected expectation remains zero. The model assumes $0 \le \gamma_e, v_i \le 1$.

Reporting noise is a classical postprocessing of the parity report. Writing v_i as a product of participating-site factors is an error budget model; it does not require destructive local measurements on the retained memory. For path queries and site rates p_j, $v_i = \prod_{j \in \mathrm{supp}(K_i)} (1 - 2p_j)$ has at most three factors. The nonselective detector contract and the noisy report remain distinct specifications.

D.2 Dynamic programming

After deciding the first i sites, retain the best partial score for each current run length $\ell \in \{0, \dots, k\}$. When choosing the next bit $b \in \{0, 1\}$, finalize the previous site's contribution

$$\mathbf{1}\{\ell > 0\}\, w_i v_i\, \gamma_{i-1}^{\mathbf{1}\{\ell \ge 2\}}\, \gamma_i^b.$$

The new length is $\ell + 1$ for $b = 1$ and zero for $b = 0$. Reject lengths exceeding k, and append a final zero to close the last run. Optimal substructure follows because future contributions depend only on the current run length. This gives $O(dk)$ transitions; backpointers give an implementation without growing-mask arithmetic. Our small-instance implementation retains integer masks for deterministic ties, whose bit-operation cost is additional to the transition count. The all-odd control rejects a zero that closes a positive even run. The primary family requires only one odd run: retain an additional Boolean flag, set it whenever a positive odd run closes, and accept only final states with that flag set. Even runs remain allowed. This doubles the state count and preserves the $O(dk)$ transition bound.

An independent verifier uses interval scheduling: at site i, either skip it, or retain a run of allowed length ℓ and continue after its separator. It explicitly sums that run's weighted noisy contrasts.

Agreement of these two recurrences checks optimization separately from direct Born-rule evaluation of the physical model.

D.3 Information equality after preparation errors

For a retained odd component B, let $W_B = \prod_{i\in B} K_i$. The codeword before noise satisfies $W_B|\psi_g\rangle = (-1)^{g|B|}|\psi_g\rangle = (-1)^g|\psi_g\rangle$. Every retained-edge ZZ commutes with W_B, since it flips two constituent stabilizer signs. The noisy codewords remain in opposite W_B eigenspaces. They therefore preserve the exact classical experiment G, including for mixed noisy states. One odd component suffices; requiring all components odd is a clean stronger control. The support argument permits correlated mixtures or coherent operations generated by the ZZ errors, although the contrast product assumes independent errors.

A fixed nonempty architecture is required. A hidden mixture over architectures can have different distinguishing observables and need not preserve the bit. In the experiment, training selects one architecture and records it before future trials. For an even two-site component, $\tau_g' = (1-p)\tau_g + p\tau_{1-g}$, so the codewords overlap at $0 < p < 1/2$. At $p = .2$, their trace overlap is .32. This counterexample is retained beside the odd-code control.

E A sharp path law when entanglement depth grows

All reports in this section are sharp. The comparator is the full depth-k physical encoder class of Section 4, not the one-odd circuit family used for noisy preparation. All logarithms in rates and divergences are natural.

Theorem 3 (Growing entanglement depth on a path)**.** *For $d \geq 3$, $2 \leq k \leq d-1$, and $m \geq 1$,*

$$\frac{D}{128k}\min\left\{1, \sqrt{\frac{d\log(k+1)}{m}}\right\} \leq \mathfrak{M}_m(P_d, k) \leq \frac{16D}{k}\min\left\{1, \sqrt{\frac{d\log(k+1)}{m}}\right\}. \tag{14}$$

The constants are uniform in d, k, m. The upper bound is attained by a learner returning information-preserving codes. Its empirical optimization costs $O(d)$ arithmetic operations after counting the requests. The lower bound permits arbitrary mixed physical encodings. For $k \geq d$, allocation excess is zero.

E.1 Upper bound: the oracle sacrifices little mass

A feasible indicator leaves no selected run longer than k. Write J for its deleted vertices and $\ell_J(i) = \mathbf{1}\{i \in J\}$. For an inclusion-minimal deletion set with t vertices, let $l_0, \ldots, l_t$ be its intervening selected-run lengths, including possibly empty endpoint runs. Minimality implies $l_{j-1} + l_j \geq k$ at each deleted vertex. Hence $tk \leq 2\sum_j l_j = 2(d-t)$, or $t \leq 2d/(k+2)$. If N is the number of these deletion sets and $q = \lfloor 2d/(k+2)\rfloor \leq d/2$, then

$$\log N \leq \log \sum_{j=0}^{q}\binom{d}{j} \leq q\log(ed/q) \leq \frac{4d}{k}\log(k+1).$$

Deleting one residue class modulo $k+1$ is feasible. Averaging its deleted workload mass over the $k+1$ offsets shows that the optimal deletion loss $r_* = \min_J \pi(J)$ is at most $1/(k+1)$.

Let J_* minimize population deletion loss and let $\widehat{J}$ minimize empirical deletion loss over the minimal deletion sets. For a fixed candidate with excess $\delta = \pi(J) - r_* > 0$, put $Z = \ell_J(T) - \ell_{J_*}(T)$. Then $\mathbb{E}Z = \delta$, $|Z| \leq 1$, and $\operatorname{Var} Z \leq \delta + 2r_*$. Bernstein's inequality therefore gives the conservative bound

$$\Pr(\widehat{\pi}(J) \leq \widehat{\pi}(J_*)) \leq \exp\left(-\frac{m\delta^2}{4r_* + 4\delta}\right).$$

For $x = \log N + t$, a union bound implies

$$\Pr\left(\pi(\widehat{J}) - r_* > \frac{4x}{m} + 2\sqrt{\frac{r_* x}{m}}\right) \leq e^{-t}.$$

Integration of this tail, followed by Jensen's inequality, yields

$$\mathbb{E}[\pi(\widehat{J}) - r_*] \le \frac{4(\log N + 1)}{m} + 2\sqrt{\frac{r_*(\log N + 1)}{m}}.$$

Since $\log N + 1 \le (5d/k)\log(k+1)$, writing $x = d\log(k+1)/m \le 1$ bounds this expectation by $(20x + 2\sqrt{5}\sqrt{x})/k \le 25\sqrt{x}/k$. Binary prediction excess is $D/2$ times deletion excess. When $x > 1$, instead sample a uniform periodic deletion offset; its expected excess is at most $D/[2(k+1)]$. These two learners give the stated upper bound, with a choice determined by known d, k, m.

For empirical optimization, add virtual deleted positions $0, d+1$ of weight zero. A valid next deletion lies at distance at most $k+1$. The shortest-path recurrence is

$$f(j) = w_j + \min_{\max(0,j-k-1)\le i<j} f(i).$$

A monotone deque maintains the sliding minimum in amortized constant time per vertex. Optimize lexicographically by deletion weight and then number of real deleted vertices. Any removable zero-weight deletion would improve this second objective, so the resulting set is inclusion-minimal. Backtracking takes $O(d)$ time. Each selected indicator has the lossless projector code of Theorem 1; no odd-component restriction is needed in this noiseless construction.

E.2 Lower bound: identify the least requested query

Set $r = \lfloor (d+1)/(k+2) \rfloor \ge d/(4k)$. Place r disjoint $(k+1)$-vertex path segments, separated by single zero-weight vertices. All unused vertices also have weight zero. In segment j, one unknown vertex $U_j \in \{1, \dots, k+1\}$ has weight $(1 - k\theta)/[r(k+1)]$; each other vertex has weight $(1+\theta)/[r(k+1)]$. Choose

$$\theta = \min\left\{ \frac{1}{2k}, \sqrt{\frac{r\log(k+1)}{8mk}} \right\}.$$

These workloads are nonnegative and sum to one. Each physical contrast projects into the product of the segment polytopes $\{c \in [0,1]^{k+1} : \sum_i c_i \le k\}$: a full connected segment cannot fit in a depth-k block, and every proper subset is feasible. Decompose each projected contrast into a randomized indicator and complete it to exactly k selected vertices per segment, setting every connector to zero. This transformation depends on the learner's output but not on the unknown workload. It gives a randomized feasible physical indicator whose conditional expected score is no smaller for every workload in the construction. The unique omitted vertex in each segment is therefore an estimate $\widehat{U}_j$. Every error $\widehat{U}_j \ne U_j$ costs excess $D\theta/(2r)$.

Give the U_j independent uniform priors. To bound the information about one coordinate, reveal all the other coordinates. Compare each resulting request distribution with an auxiliary distribution that makes segment j uniform and leaves the other segments unchanged. Its one-sample chi-squared divergence is $k\theta^2/r$. KL is no greater, so the information in m requests about U_j, even with the revealed coordinates, is at most $mk\theta^2/r \le \log(k+1)/8$. Fano's inequality (Yu, 1997) gives

$$\Pr(\widehat{U}_j \ne U_j) \ge 1 - \frac{1}{8} - \frac{\log 2}{\log(k+1)} \ge \frac{1}{8}.$$

Thus Bayes excess, and hence minimax excess, is at least $D\theta/16$. The bound $r \ge d/(4k)$ gives

$$\theta \ge \frac{1}{\sqrt{32}\,k} \min\{1, \sqrt{d\log(k+1)/m}\},$$

which implies the stated constant $1/128$.

The theorem distinguishes absolute error from resolving the remaining allocation choices. Depth k reduces worst-case excess to order $1/k$, even without requests. Learning a sufficiently small fixed fraction of that scale requires order $d\log(k+1)$ requests. The fixed-depth path law is recovered when k is held constant.

Relation to sparse-loss prediction. When $k = d - 1$, every maximal allocation omits one vertex. A query then assigns loss one to its own omission action and zero to every other action: the loss vector is one-hot. This is the sparse-loss setting studied by Kwon & Perchet (2016). Their full-information regret bound (Theorem 4) gives $O(\sqrt{m \log(d)/d + \log d})$ for this case; online-to-batch conversion recovers the large-sample upper rate $O(\sqrt{\log(d)/(dm)})$ when $m \geq d \log d$. The small-loss improvement is therefore a classical ingredient. Our theorem handles coupled deletion choices at every depth, gives uniform finite-sample bounds, constructs physical attaining encodings, and includes arbitrary mixed encoders in its lower bound.

F Completing an empirical allocation

Let $\mathcal{A}$ be a finite downward-closed family of query sets, with nonnegative empirical weights $\widehat{w}$ and population weights w. If $\widehat{S}$ maximizes empirical weight over $\mathcal{A}$, every feasible inclusion-maximal extension $M \supseteq \widehat{S}$ satisfies

$$\widehat{w}(M) = \widehat{w}(\widehat{S}), \qquad w(M) \geq w(\widehat{S}).$$

The first claim follows because a strict increase would contradict empirical optimality; the second follows from nonnegativity. Every added coordinate has zero empirical weight. Consequently, full-feasible and maximal-set ERM are not intrinsically different statistical problems. The smaller maximal class gives a tighter analysis and a useful tie rule. A poor tie rule can nonetheless create an arbitrarily large sample-requirement penalty.

For an exact example, take $K_{a,a}$ at depth one, with total probabilities $3/4$ and $1/4$ on the two colors, uniform within each color. Let $K \sim \mathrm{Binomial}(m, 3/4)$ and break color ties toward the first color. An ERM retaining only observed vertices of the winning color has expected captured mass

$$\mathbb{E}\left[\mathbf{1}\{2K \geq m\}\frac{3}{4}\{1 - (1 - 1/a)^K\} + \mathbf{1}\{2K < m\}\frac{1}{4}\{1 - (1 - 1/a)^{m-K}\}\right].$$

Its excess is $(D/2)(3/4 - \text{expected captured mass})$. Completing the winning color instead has expected excess $(D/4)\Pr(2K < m) \leq (D/4)e^{-m/8}$, independent of a. The sparse rule's excess is at least $(3D/8)(1 - m/a)$. The experiment compares these exact expectations with independently sampled counts; it does not claim a new minimax separation between the two feasible classes.

G Two statistical resources under preparation noise

Let $\mathcal{A}$ be the finite one-odd path circuit family, of size N, and let $b_i(S) = \mathbf{1}\{i \in S\} v_i \prod_{e \ni i,\ e \text{ retained}} \gamma_e$. Calibration supplies B independent Bernoulli observations for each edge error probability and each native report-success probability. Clip the resulting estimates of γ_e and v_i to $[0, 1]$. The learner maximizes $\widehat{\pi} \cdot \widehat{b}(S)$ using m independent request identities, independently of calibration. Suppose the true effective contrasts $b_i^{\mathrm{true}}(S) \in [0, 1]$ also satisfy

$$\sup_{S \in \mathcal{A}} \sum_i \pi_i |b_i^{\mathrm{true}}(S) - b_i(S)| \leq \beta.$$

The mismatch condition concerns prediction contrasts. It does not assert information preservation under an unspecified true channel. We define its Bayes risk as $R_\pi^{\mathrm{true}}(S) = 1/2 - (D/2)\pi \cdot b^{\mathrm{true}}(S)$; the proposition does not bound an arbitrary estimated decoder.

Proposition 1 (Requests, calibration, and model error)**.** *For the raw empirical maximizer, expected excess over the best member of the same circuit family under the true contrasts obeys*

$$\mathbb{E}[R_\pi^{\mathrm{true}}(\widehat{S}) - \min_{S \in \mathcal{A}} R_\pi^{\mathrm{true}}(S)] \leq D \min\left\{\frac{1}{2}, \sqrt{\frac{\log(2N)}{2m}} + \frac{3}{\sqrt{B}} + \beta\right\}. \tag{15}$$

The calibration cost is $B(2d - 1)$ scalar observations, in addition to the m requests.

Proof. Conditional on calibration, each function $i \mapsto \widehat{b}_i(S)$ takes values in $[0, 1]$. The exponential-moment form of Hoeffding's inequality gives expected uniform request deviation at

most $\sqrt{\log(2N)/(2m)}$. Telescoping products in $[0,1]$ gives

$$|b_i(S) - \widehat{b}_i(S)| \le |v_i - \widehat{v}_i| + \sum_{e \ni i} |\gamma_e - \widehat{\gamma}_e|.$$

Clipping cannot increase estimation error. Each estimated factor has expected absolute error at most $1/\sqrt{B}$, by its binomial variance and Cauchy–Schwarz. Each query has at most two incident edges, so the expected workload-weighted deviation is at most $3/\sqrt{B}$. Adding model mismatch gives the displayed sum as an expected uniform score error. Empirical maximization costs at most twice that error; conversion to risk multiplies by $D/2$. All true contrasts lie in $[0,1]$, so excess is also at most $D/2$. □

The guarantee has no sharp claim about constants or graph-dependent calibration complexity. It is for raw counts; the smoothed methods are separately evaluated estimators. For half-count smoothing of request counts, with calibration estimates unchanged, the same proof adds a deterministic score perturbation at most $d/(2m+d)$ inside the parentheses. This bound is deliberately conservative and need not certify a small observed improvement.

G.1 A SHARP JOINT LAW ON DEPTH-THREE PATHS

The two terms in Proposition 1 cannot in general replace one another. Let $\mathcal{A}_3$ be the same one-odd path circuit family with depth cap three. Write

$$\mathfrak{J}_{m,B}(d) = \inf_{\widehat{S}} \sup_{\pi,\gamma,v} \mathbb{E}\left[R_{\pi,\gamma,v}(\widehat{S}) - \min_{S \in \mathcal{A}_3} R_{\pi,\gamma,v}(S) \right],$$

where the learner observes m request identities and B independent Bernoulli observations for each edge and native visibility, as above. The supremum is over all workloads and factors in $[0,1]$; D is fixed and $\beta = 0$. The learner may randomize its allocation. The comparator and learner both belong to $\mathcal{A}_3$.

Theorem 4 (Joint request and calibration complexity)**.** *For $d \ge 4$ and $m, B \ge 1$,*

$$\frac{D}{256} \min\left\{1, \sqrt{d/m} + B^{-1/2}\right\} \le \mathfrak{J}_{m,B}(d) \le 3D \min\left\{1, \sqrt{d/m} + B^{-1/2}\right\}. \tag{16}$$

Proof. The upper bound follows from Proposition 1 with $N \le 2^d$ and $\beta = 0$.

For the request lower bound, set $\gamma = v = 1$ and place $r = \lfloor (d+1)/5 \rfloor \ge d/8$ four-vertex subpaths along the path, separated by unused vertices. Each gadget has one of two possible low-probability vertices. Its low vertex has probability $(1-3\theta)/(4r)$; its other three vertices have probability $(1+\theta)/(4r)$, where $\theta = \frac{1}{8}\min\{1, \sqrt{r/m}\}$. All remaining queries have probability zero. A feasible allocation retains at most three vertices of each gadget. Every choice of three is attainable by omitting the separators: three selected vertices on a four-vertex path always include an odd run. Thus the oracle that omits every low vertex belongs to $\mathcal{A}_3$.

Replace a learner's allocation by completing its projected set to three vertices per gadget and setting every other coordinate to zero. The replacement is feasible and cannot decrease its score for any workload in the construction. Map its omitted vertex to the corresponding low-vertex guess; if it omits neither candidate, choose either guess. A wrong guess costs at least $D\theta/(2r)$ in excess risk. Flipping one gadget's low vertex changes the one-request distribution by KL divergence

$$\frac{\theta}{r} \log \frac{1+\theta}{1-3\theta} \le \frac{8\theta^2}{r}.$$

The m-sample KL is at most $1/8$, so Pinsker's inequality bounds neighboring total variation by $1/4$. Averaging over all sign vectors, each guess errs with probability at least $3/8$. The total excess is at least $3D\min\{1, \sqrt{r/m}\}/128$, hence at least $D\min\{1, \sqrt{d/m}\}/128$. Calibration data are deterministic here and reveal nothing about the unknown workload.

For the calibration lower bound, put probability $1/3$ on each of the first three queries and zero elsewhere. Set $v = 1$ and all edge factors except the first two to one. Those two factors are both

$\gamma_\pm = \sqrt{3} - 1 \pm \delta$, where $\delta = 1/(16\sqrt{B})$. On the active subpath, every pattern except 111 and 101 is dominated by 101 for both parameter values. Set all outside coordinates to zero and replace every active prefix other than 111 by 101. Both resulting allocations are feasible, have an odd run, and weakly improve the original score in both worlds. The outside edge factors equal one, so removing outside vertices does not change active contrasts. Their score difference is

$$f(\gamma) = \frac{2\gamma + \gamma^2 - 2}{3}, \qquad |f(\gamma_\pm)| \geq \delta.$$

Thus the preferred allocation changes with the sign, and a wrong choice costs at least $D\delta/2$.

Only two edge-calibration panels carry information about the sign. Their Bernoulli parameters are $(1 - \gamma_\pm)/2$ and differ by δ. Both lie between 0.10 and 0.17, so each observation has KL at most $12\delta^2$. The full calibration KL is at most $24B\delta^2 = 3/32$ and total variation is less than $1/4$. Request observations have the same distribution in both cases. The two-point testing bound therefore gives expected excess at least $3D\delta/16 = 3D/(256\sqrt{B})$. Randomized allocations obey the same bound: dominated patterns can be replaced by 101, leaving a randomized choice between the two candidates.

Taking the larger of the request and calibration lower bounds proves the stated sum bound, using $\max\{\min(1, a), b\} \geq \frac{1}{2}\min(1, a + b)$ for $a \geq 0$ and $0 \leq b \leq 1$. □

The rate is sharp for this path family, not the displayed constants. Since total calibration cost is $Q = B(2d-1)$, its second term is $\sqrt{(2d-1)/Q}$. The theorem fixes the per-parameter sampling scheme; it does not rule out gains from adaptive calibration or additional shared structure in a particular device's parameters.

H Experimental protocols and complete comparisons

This appendix documents the population-risk experiments. The request/calibration, online and noise protocols were specified before their draws. The geometry and connected-region studies retain their original observations; the later port-repair comparison reuses those observations and is retrospective. The archive contains the protocols, source hashes, raw arrays and complete analyses. Physical acquisitions are reported separately in Appendices N and O.

H.1 Growing-depth scaling diagnostic

A separate protocol varies $d \in \{128, 256, 512, 1024\}$ and $k \in \{2, 4, 8, 16, 32\}$, with sharp reports and $h = 0$. Rounded request budgets are $m = d\log(k+1)\{1/8, 1/2, 2, 8, 32, 128\}$. Each dimension/depth/family condition has 64 independent seeds, for 15,360 empirical fits across two workload families. The local-alternative family uses the exact separated-segment construction and budget-dependent θ in Appendix E; its low-query identities remain fixed across budgets but its probabilities change. The fixed-workload control draws $\pi \sim \mathrm{Dirichlet}(0.5, \ldots, 0.5)$ and uses nested request prefixes. The empirical learner minimizes omitted count, then number of omissions, with the linear-time recurrence. The oracle knows the workload; a uniform periodic allocation supplies a data-free comparator. All are evaluated by exact population risk in the full ideal depth-k family.

Figure 2 presents both families in the main text.

For normalized budgets at least two, $k\sqrt{m/[d\log(k+1)]}$ times empirical excess ranges from 0.0656 to 0.1578 across all hard-family cells. At the largest budget it ranges from 0.0028 to 0.0071 on fixed Dirichlet workloads. The latter are not minimax-hard populations. The periodic baseline shares the hard-family slope because θ decreases with m. Only the fixed-workload control tests learning on unchanged populations. All dimension-specific curves, bootstrap intervals, masks, counts and periodic baselines are retained. Before acquisition, 744 exhaustive or independent-recurrence objectives passed; every fitted mask and population risk was subsequently replayed. Acquisition took 8.63 seconds with one numerical thread, excluding verification and plotting. The curves test the proved rate on its constructed families; their slopes do not define a universal learning exponent.

H.2 Fixed-depth geometry comparisons

The retained fixed-workload experiments compare paths with bicliques and vary the number and size of connected regions (Figure 6). Section 6.1 reports their population-risk interpretation and stronger repair controls.

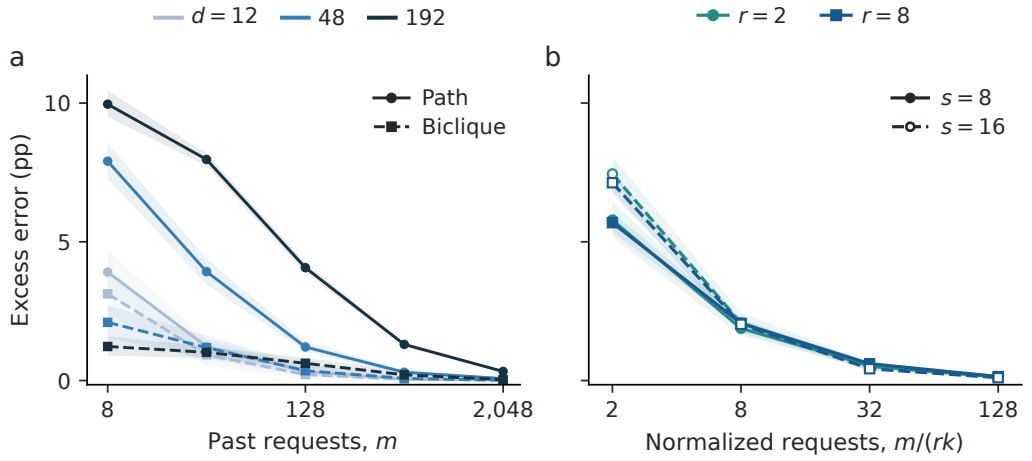

Figure 6: Enlarging a region differs from adding allocation decisions. (a) Fixed full-support Dirichlet workloads on paths and bicliques, at depth two; 20 paired workload instances with ten training repetitions. (b) Chains of r biclique regions, each with s vertices per color, at depth four and total connection-query mass 0.2; 24 paired fixed instances with ten repetitions. Population excess is measured against the physical-class optimum; bands are pointwise 95% instance-bootstrap intervals. Reports are sharp and $h = 0$. These fixed-workload curves do not estimate minimax rates; biclique query support grows with s.

H.3 Two-resource factorial design

For each $d \in \{63, 127\}$ and each of three noise regimes, draw 32 independent workload/channel instances. Requests have $\pi \sim \mathrm{Dirichlet}(0.5, \ldots, 0.5)$. To generate native query visibility, draw local outcome-error probabilities uniformly from $[0.002, 0.02]$ and multiply their $1 - 2e$ factors over the path query's two or three sites. Calibration observes each resulting native visibility directly; it does not estimate those underlying local errors. Low preparation noise has independent edge-error probabilities uniform in $[0.001, 0.01]$. Heterogeneous noise replaces an independently marked quarter of edges by errors uniform in $[0.08, 0.18]$. Stress noise uses $[0.2, 0.4]$ on the marked edges. These are controlled synthetic distributions, not fitted device noise.

Each instance has four request streams and four independent calibration panels. Request budgets are the rounded positive integers $m = d\{1/4, 1, 4, 16, 64\}$; calibration budgets are $B \in \{4, 16, 64, 256, 1024\}$ per parameter. Independent multinomial increments give nested request prefixes. Independent binomial increments give nested edge-error and native-report-success counts. The two sources are independent and crossed, producing $192 \cdot 5 \cdot 5 \cdot 4 \cdot 4 = 76{,}800$ fitted rows per method. The two prefix axes pair the learning curves; they do not increase the number of independent workload/channel units.

Edge counts estimate $\gamma_e = 1 - 2\epsilon_e$ and native successes estimate $(1 + v_i)/2$. Clip both estimated factors to $[0, 1]$. Total calibration is $Q = B(2d - 1)$, separately from m requests. At the two dimensions, $B = 256$ costs 32,000 and 64,768 scalar observations. The study does not supply a physical exchange rate between calibration, request acquisition, detector operations and preparation gates. Its mean gate counts concern one preparation.

Table 1: Matched estimators isolate the value of calibration. Population error and mean preparation CZ counts in the prespecified 63-qubit cell ($m = 1{,}008$, $B = 256$). Intervals are pointwise 95% bootstrap intervals over 32 workload/channel instances. The oracle knows the true workload and channel. Allocation rows have depth at most three and an odd run; Product has depth one and Full chain depth 63.

Design	Error (%) [95% interval]	Mean CZ gates
Joint, smoothed	8.58 [8.19, 8.99]	22.3
Task only, smoothed	9.79 [9.24, 10.37]	25.8
Joint, raw	8.62 [8.24, 9.03]	19.5
Task only, raw	9.62 [9.09, 10.17]	22.6
Reporting only, smoothed	9.77 [9.23, 10.34]	25.8
Greedy, smoothed	8.94 [8.45, 9.50]	22.3
Product, smoothed	15.64 [15.06, 16.22]	0.0
Full chain	9.54 [8.91, 10.16]	62.0
Workload and channel oracle	8.32 [7.96, 8.71]	21.5

H.4 Matched estimators and privileged diagnostics

Joint uses empirical requests and both estimated channel factors. Task only sets both factors to one. Each is evaluated using raw frequencies and half-count smoothing, $\widetilde{\pi}_i = (n_i + 1/2)/(m + d/2)$, with calibration unchanged. Reporting only uses smoothed requests, estimated native visibility, and ideal preparation factors. Joint, Task only and Reporting only use the same dynamic program and first-predecessor tie rule. The selected runs may have length one, two or three; at least one run must be odd.

Greedy starts with the greatest standalone-benefit singleton and visits the remaining sites in descending estimated standalone benefit. It accepts an addition only if it strictly raises estimated score and keeps the same one-odd feasible family. This is a one-pass heuristic, not a local optimum: a beneficial multi-site addition can be missed when its intermediate single-site additions violate the odd condition. Product solves the cap-one problem with smoothed requests and native visibility. Full chain retains every site, uses depth d, and needs neither request fitting nor calibration. Its excess relative to a cap-three oracle may be negative because its resource budget differs.

Known channel uses true factors with smoothed empirical requests. Known workload uses true requests with estimated factors. The circuit oracle knows both. Their risk differences diagnose the two error sources, but need not add exactly: changing either estimate can change the selected mask. None is tuned with population outcomes. The primary comparison, fixed before the draws, is Task only smoothed minus Joint smoothed at $d = 63$, heterogeneous noise, $m = 1{,}008$, and $B = 256$.

H.5 Uncertainty, adverse cells, and depth sensitivity

Risk is evaluated exactly from the true synthetic factors after each mask is chosen. The 16 request/calibration repetitions are averaged within each latent instance. Five thousand paired bootstrap resamples of the 32 instances give pointwise 95% percentile intervals. Secondary intervals are descriptive and have no multiplicity adjustment. All 150 dimension/noise/budget cells are released, including both raw and smoothed estimators. We use population risk as the primary outcome because it is available exactly. Sampling binary outcomes from the same model would add variance without testing a different assumption.

The full 150-cell grid is in `revision/phase3/results/research90/study/analysis.json`; the extended evidence supplement prints its corner cells. The main matched-smoothed gain is 1.214 points, with paired interval $[0.947, 1.496]$. Joint's primary error is 8.576% versus the same-family oracle's 8.320%. The raw-count comparison is also reported: Joint has 8.618% error and Task only 9.616%. Smoothing improves Joint in this cell and worsens Task only. Comparing all four versions separates the effect of smoothing from the effect of learning the channel.

The prespecified depth sensitivity evaluates caps five and seven on the same 32 heterogeneous-noise instances at $d = 63$, retaining the complete budget matrix and identical request/calibration arrays. Each cap has its own true-workload, true-channel oracle. Larger capacity expands the family but need not improve a fitted estimator at every finite budget. The extended depth-sensitivity table reports the primary budget without substituting the best depth into the declared primary comparison. The full depth-sensitivity table is retained in the extended evidence supplement.

I STRONGER ALLOCATION BASELINES

I.1 SELECTIVE REPAIR OF CONNECTED ALLOCATIONS

The original connected-region study has 96 full-support cells: $r \in \{2, 8\}$, $s \in \{8, 16\}$ vertices per color, $k \in \{2, 4\}$, total connection-query mass in $\{0.05, 0.2, 0.5\}$ and $m/(rk) \in \{2, 8, 32, 128\}$. Each cell contains 24 workload instances with ten request repetitions. The repair controls use the original masks and observed outcomes.

The new retrospective control first optimizes each region independently. When a selected component exceeds the cap, it removes the lowest-count endpoint of a selected interregion edge in an oversized component. It repeats until feasible, then adds feasible queries in descending training count. A second version makes two deterministic passes of strictly improving one-for-one swaps. These rules use training counts alone, with graph connectivity checked explicitly. We evaluate all 96 original cells, without selecting workloads for their observed improvement.

At the original primary condition ($r = s = 8$, $k = 4$, connection-query mass 0.2 and $m = 1024$), exact allocation has 14.998% population error. Repair gives 15.170% and repair with local improvement 15.143%. Their paired differences from exact allocation are 0.172 points ($[0.093, 0.252]$) and 0.145 points ($[0.075, 0.220]$), compared with 5.242 points for deleting every connection query. Thus most of that earlier gap reflected the coarse connection-removal baseline. Raw masks, preparation gates and sampled future outcomes for the new controls are included in the archive.

J REPRODUCTION AND HISTORICAL EVIDENCE

The installable allocation package provides the path optimizer, Gibbs distribution and sampler, with input validation and a runnable example. Its README gives commands for a clean environment. The full reproduction entry point verifies frozen acquisition hashes, regenerates request and calibration prefixes, checks population risks and compares the main optimizer against an independent interval implementation. It also checks manuscript references and the compiled artifact.

Before acquisition, exhaustive enumeration verified 864 max-plus optimizer cases and 36 complete Gibbs distributions. The binary information bound was checked on 100,000 asymmetric channels. After acquisition, 11,136 independent interval optimizations checked the primary fitted method, and every population-risk row was recomputed. These finite checks corroborate the mathematical proofs; they do not replace them. Factorial acquisition took 50.50 seconds on six workers; controls took 179.61 seconds. Numerical libraries used one thread per worker; these times exclude development, audits, analysis and plotting. All study seeds and exact package versions are recorded in the machine-readable protocols.

The historical evidence supplement preserves the preceding full manuscript, including the two-qubit benchmark, earlier allocation studies and the 215,040-shot fixed IBM acquisition. It preserves their chronology and their original limitations. These device observations compare fixed implementations in a different measurement family; they are not evidence for learned allocation, an all-input detector guarantee, or exact information preservation in noisy device states.

K LEARNING PROBES FOR DETECTOR DIAGNOSIS

The same allocation problem governs two tasks: recovering a stored bit and detecting a change in the detector. This section establishes the connection over the full physical encoder class, then tests its limits under more general detector noise. Numerical results in this section are calculations

for declared models. Appendix O reports the prospective quantum-processor evaluation, including calibration transfer, coherence controls, and acquisition costs.

K.1 An exact diagnostic experiment for every CSS allocation class

Let $H \in \{0, 1\}$ denote healthy or faulty operation. Before each call, the client prepares a state in $\mathcal{S}_{\mathcal{F}}$, the partition class of Section 2. An independent request $T \sim \pi$ then selects one of the independent commuting CSS queries. The detector measures its ideal parity and flips the report with probability e_H, where $0 \le e_0 < e_1 \le 1$. Flips are independent across calls and of the request, preparation and ideal outcome, conditional on H. The evaluator sees the request, report and any classical preparation tag. Each state must belong to $\mathcal{S}_{\mathcal{F}}$ conditional on that tag and the complete past history. The client retains no quantum system between calls. Classical randomization, biased states and adaptation to every past report are allowed. Training requests are independent of H.

For partition Π, let I be a locally compatible set of queries, as in Theorem 1, and define

$$p_{\mathcal{F}}(\pi) = \max_{\Pi \in \mathcal{F},\ I \text{ compatible on } \Pi} \sum_{t \in I} \pi_t.$$

Write E_p for an experiment that returns an erasure with probability $1 - p$ and an observed flip bit distributed as $\mathrm{Bernoulli}(e_H)$ with probability p. Its erasure indicator is independent of H. Let $B_{p,N}(\alpha)$ be its optimal N-call detection power at false-alarm probability at most α.

For one-call learning, let $S_m \sim \pi^m$ be the training requests. A learner A maps S_m to an admissible probe, its retained classical tag, and an alarm rule. Write $\beta_\pi(A; S_m)$ for its power, averaged over preparation randomness, the new request and the report. Define

$$\mathfrak{D}_{\mathcal{F}}(m) = \inf_A \sup_{\pi \in \Delta_q} \mathbb{E}_{S_m}\left[B_{p_{\mathcal{F}}(\pi),1}(e_0) - \beta_\pi(A; S_m)\right].$$

Here A cannot use π, and its false-alarm probability must be at most e_0 conditional on every training record, tag and request. The comparator knows π. The identity below also holds if this conditional requirement is weakened to false-alarm control averaged over training and test randomness, uniformly over π.

Corollary 1 (Allocation determines diagnostic power)**.** *Under the preceding model, the optimal N-call experiment over all admissible, classically adaptive probe policies is equivalent, in Blackwell's comparison of experiments, to $\mathsf{E}_{p_{\mathcal{F}}(\pi)}^{\otimes N}$. A fixed signed projector probe supported on a maximizing I attains it. At one call and false-alarm level $\alpha = e_0$,*

$$B_{p,1}(e_0) = e_0 + (e_1 - e_0)p. \tag{17}$$

Consequently, if $\mathfrak{R}_{\mathcal{F}}(m)$ is the sharp-report minimax prediction regret of the main text, the minimax loss of one-call diagnostic power after m training requests is exactly

$$\mathfrak{D}_{\mathcal{F}}(m) = \frac{2(e_1 - e_0)}{D}\mathfrak{R}_{\mathcal{F}}(m), \qquad D > 0. \tag{18}$$

The attaining alarm has false-alarm probability e_0 conditional on every training record, preparation tag and request; it does not require knowledge of π.

Proof. The signed single-state expectation region is the convex hull of $s \odot \mathbf{1}_I$, where I ranges over compatible sets and $s_t \in \{-1, +1\}$. For the outer bound, the main theorem's single-state cut inequalities bound absolute correlations. For attainment, the normalized signed projector

$$\tau_s^I = 2^{-d} \prod_{t \in I} (I + s_t P_t)$$

is separable across the chosen partition. Independence of the global Paulis makes its expectation s_t on I and zero off I. Thus every admissible state's entire report channel is a mixture of these vertex channels under both hypotheses. This is a channel decomposition; it need not decompose the original density matrix. Revealing the mixture component can only help the evaluator.

A vertex gives a known ideal report on I and a fair, hypothesis-independent report otherwise. Its experiment is $\mathsf{E}_{\pi(I)}$: the remaining request identity and known sign are ancillary conditional on the

informative flag and flip bit. If $p' \le p$, erase an informative output of E_p with probability $1 - p'/p$ to obtain $\mathsf{E}_{p'}$. Draw a compatible query identity from its conditional distribution and restore its known sign to reproduce the full vertex channel. The resulting kernel never uses H. Applied conditionally on the simulated history at each call, it reproduces every adaptive policy from independent copies of $\mathsf{E}_{p_{\mathcal{F}}}$. The maximizing fixed vertex attains this experiment, proving optimality for every terminal test.

For Eq. (17), alarm on an informative flipped report, never alarm on an informative unflipped report, and alarm with independent probability e_0 on an erasure. Its false-alarm probability is e_0 even conditional on the request. Its power is $e_0 + (e_1 - e_0)p$. Conversely the total variation between the two one-call laws is $(e_1 - e_0)p$, so no level-e_0 test has greater power.

More generally, a conditional state with expectations r_t has one-call total variation $(e_1 - e_0) \sum_t \pi_t |r_t|$. Averaging over training and retained tags preserves this upper bound. The mean absolute-correlation vector remains in the main theorem's convex feasible region. Every vector in that region is realized by a tagged mixture of signed projectors, with the preceding alarm attaining the bound. Prediction regret is $D/2$ times the loss of weighted coverage; diagnostic-power regret is $e_1 - e_0$ times that same loss. Taking the same infimum over learners and supremum over workloads proves Eq. (18). □

In particular, the path law becomes $\Theta((e_1 - e_0)k^{-1} \min\{1, \sqrt{d \log(k+1)/m}\})$, uniformly over $2 \le k < d$. The connected-region law transfers with the same geometric conditions. This is a learning result for probe allocation: the hypotheses e_0, e_1 are known. Estimating a healthy baseline or an operating threshold costs separate calibration data.

For arbitrary N, a learned compatible set of mass $\widehat{p}$ also satisfies the same-level transfer bound

$$0 \le B_{p^*,N}(\alpha) - B_{\widehat{p},N}(\alpha) \le 1 - \{1 - (e_1 - e_0)(p^* - \widehat{p})\}^N.$$

To see this, promote erased outputs of $\mathsf{E}_{\widehat{p}}$ to informative outputs with probability $(p^* - \widehat{p})/(1 - \widehat{p})$ and generate their flip bits using e_0. Under $H = 0$ this exactly reproduces E_{p^*}; under $H = 1$ the one-use total-variation error is $(e_1 - e_0)(p^* - \widehat{p})$. Product coupling gives the bound. It compares optimal population tests, not estimated thresholds.

L THE COST OF CHANGING THE DETECTOR INTERFACE

Extra calls can match an entangled probe's diagnostic performance. To determine their cost, we compare the complete statistical experiments. Let E_p denote the experiment with probabilities

$$P_h(\perp) = 1 - p, \qquad P_h(0) = p(1 - e_h), \qquad P_h(1) = pe_h,$$

where $h \in \{0, 1\}$ indexes detector health, $0 < e_0 < e_1 < 1$, and the informative flag is observed. The nonerased bit records whether the reported sign disagrees with the prepared sign. We use Blackwell equivalence under both hypotheses throughout this section. It requires more than matching power at one operating point.

L.1 FRESH REQUESTS AND OPTIMAL EXPECTED CALL CONVERSION

Theorem 5 (Exact fresh-call conversion)**.** *Suppose every admissible fresh call, conditional on its preceding classical history, is dominated by E_p, and some fixed admissible probe attains E_p. A fresh probe precedes each new independent request; no quantum system is retained between calls. For $0 < p \le q \le 1$, any terminating policy whose output dominates $\mathsf{E}_q^{\otimes N}$ uses at least Nq/p calls in expectation under each hypothesis. A stopped policy attains equality and produces an equivalent complete experiment.*

Proof. Write $d_h = D_{\mathrm{KL}}(\mathrm{Bern}(e_h) \| \mathrm{Bern}(e_{1-h}))$. Conditional one-call domination bounds the KL increment by pd_h. The chain rule for a stopped transcript, first at a truncated horizon and then by monotone convergence, gives

$$D_{\mathrm{KL}}(P_h^{\mathrm{transcript}} \| P_{1-h}^{\mathrm{transcript}}) \le pd_h \, \mathbb{E}_h \tau.$$

The action and stopping kernels are functions of the observed history, so they add no likelihood ratio. By data processing, the target experiment requires the left side to be at least Nqd_h. Dividing proves the lower bound. Infinite expected cost satisfies it trivially.

For one target output, make a fresh call. Return an informative bit if obtained. Following an erasure, with probability $(q-p)/(1-p)$ restart until the first informative bit; otherwise return an erasure. The informative probability is q and expected cost is $1+(q-p)/p = q/p$. Conditional on the output, the discarded erasures and stopping details are independent of health. The full transcript is therefore equivalent to E_q. Independent repetition proves the claim for N outputs. The case $p = 1$ is trivial. □

For the menu (ZZI, XXX, IZZ) with probabilities $(.2, .6, .2)$, the separable and Bell coverages are .6 and .8. Here a bounded construction suffices: after an erased first product call, make one fresh second attempt with probability $5/6$ and then stop. Its coverage is $.6 + .4(5/6)(.6) = .8$, and its expected cost is $4/3$. For N target outputs the cost is $N + \mathrm{Binomial}(N, 1/3)$, with maximum $2N$. The expectation is $4N/3$ calls; the policy may exceed that number on a particular run.

At a fixed fresh horizon M, the sufficient statistic is the number K of informative calls and the number J of flips:

$$P_h(K=k, J=j) = \binom{M}{k} p^k (1-p)^{M-k} \binom{k}{j} e_h^j (1-e_h)^{k-j}.$$

Sorting these atoms by likelihood ratio and randomizing at the boundary gives exact Neyman–Pearson power. At $(e_0, e_1) = (.02, .164)$, 80% power at 5% false alarms requires 30 fresh product calls or 22 Bell calls. This finite-horizon ratio is $30/22$. Equal expected informative counts alone do not imply equivalence. The ratio q/p also compares fixed-false-alarm Stein exponents, since $D_{\mathrm{KL}}(\mathsf{E}_p^0 \| \mathsf{E}_p^1) = pd_0$. Equal-prior Bayes error instead has Chernoff exponent

$$-\log\left[1 - p + p \min_{0 \le s \le 1} \{e_0^{1-s} e_1^s + (1-e_0)^{1-s}(1-e_1)^s\}\right],$$

whose Bell/product ratio is 1.33860 at these parameters.

L.2 Chosen extra queries and retained probes

Prepare $|+++\rangle$ and serve the first random request. If it is XXX, its ideal sign is known. After either unsupported Z request, ask for XXX with probability u. All three observables commute, so every branch of the first ideal parity measurement preserves the XXX sign. The unsupported first report is fair under either health hypothesis. The complete experiment is therefore $\mathsf{E}_{.6+.4u}$, at $1 + .4u$ expected calls per original probe. In particular, $u = 1/2$ reproduces the Bell experiment at 1.2 expected calls. More generally, a supported commuting repair query gives coverage q at cost $1 + q - p$. This is an attainable policy, not an optimum over all adaptive ones. Chosen-query control matters as well as retention: a newly prepared product eigenstate queried through a chosen supported observable also achieves this call count, but consumes an additional preparation.

Keeping the probe also makes a different signal available. Repeat an unsupported nondemolition Z query. If its unknown ideal parity is S and the report flips are F_1, F_2, then

$$Y_1 = S \oplus F_1, \quad Y_2 = S \oplus F_2, \quad Y_1 \oplus Y_2 \sim \mathrm{Bern}(\theta_h), \qquad \theta_h = 2e_h(1-e_h).$$

Each report alone is fair, but their disagreement diagnoses detector noise. The stored sign remains unknown. This is why the one-call identity between prediction and diagnostic regret need not hold when a policy retains the probe.

Keep the first report on XXX and repeat the first query otherwise. For N original probes, let K count unsupported requests, J count flips on the supported first requests, and V count disagreements. The exact likelihood is

$$P_h(k,j,v) = \binom{N}{k} .4^k .6^{N-k} \binom{N-k}{j} e_h^j (1-e_h)^{N-k-j} \binom{k}{v} \theta_h^v (1-\theta_h)^{k-v}.$$

At the same known-channel 5% false-alarm level, 14 probes give 80.2647% power; 13 give 78.8579%. The 14-probe policy uses 19.6 calls on average and at most 28. It exceeds 22 calls with probability 5.8319%, so it is not a hard-budget counterexample to a 22-call comparison. Independent 8×8 instrument calculations verify the transcript factorizations to 1.2×10^{-16}.

L.3 Preparation, calls, and calibration

Let S_a be policy a's startup cost, including workload collection, response fitting, threshold calibration and setup. Let $V_a(h)$ be its expected operating cost per diagnostic episode under health h, including every preparation, detector call, report, reset, control operation and retained-state holding cost. To combine these costs, assign a price to each operation and count it once. Over L episodes, entanglement is cheaper precisely when

$$S_{\mathrm{ent}} - S_{\mathrm{sep}} < L\{V_{\mathrm{sep}}(h) - V_{\mathrm{ent}}(h)\}. \tag{19}$$

Both policies must meet the same performance requirement and use the same expected or hard resource convention. With a uniform call price and preparation-CZ price, equal other costs reduce this to $\kappa_{\mathrm{call}}(N_{\mathrm{sep}} - N_{\mathrm{ent}}) > \kappa_{\mathrm{CZ}}(G_{\mathrm{ent}} - G_{\mathrm{sep}})$, where G counts *all* preparation CZs in the episode.

Table 2: Known-channel policies reaching 80% power at 5% false alarms. Calls and gate counts are expectations; retained policies have larger hard maxima. CNOT counts are logical and exclude calibration.

Policy	Preparations	Calls	Total CNOTs
Fresh product	30	30	126.0
Bell	22	22	114.4
Fresh stopped Bell simulation	$29\frac{1}{3}$	$29\frac{1}{3}$	123.2
Product, half repair	22	26.4	114.4
GHZ	18	18	111.6
Product, full repair	18	25.2	111.6
Product, repeat unsupported query	14	19.6	75.6

The repeated-query policy can therefore be cheaper than GHZ. If each call has overhead x in units of one logical CNOT, its operating cost is $19.6x + 75.6$, versus $18x + 111.6$ for GHZ. GHZ is cheaper exactly when $x > 22.5$, before any extra startup cost. These are two attaining policies, not an optimized adaptive frontier. The physical GHZ and Adaptive-Z studies in Appendix O use different threshold calibrations; their observed powers cannot be inserted into this common-operating-point comparison without a new experiment.

M Transaction locality as an allocation problem

An allocation problem also arises when a database must decide which records to store together before seeing the next transaction. For record partition P and transaction footprint F_t, define $\ell_t(P) = \mathbf{1}\{F_t \text{ lies in one shard}\}$. The objective is $L_\pi(P) = \sum_t \pi_t \ell_t(P)$, under a record-capacity constraint and without replication. The learner maximizes empirical locality using a log of transaction identities. The cost $1 - L_\pi(P)$ is the distributed-transaction fraction. It does not by itself measure throughput or latency.

Schism formulates the transaction hypergraph objective in its Appendix B, then uses a tuple coaccess graph under balance constraints (Curino et al., 2010). Our graph vertices are queries, and deleting a vertex sacrifices a query requirement. These graphs encode different decisions. A single transaction touching two records has locality zero at shard capacity one, whereas deleting one endpoint of its tuple graph retains positive vertex weight. We therefore need an explicit construction to transfer the learning law.

Corollary 2 (Classical transaction instances)**.** *For adjacent-pair transactions on $q + 1$ ordered records, shard capacity $k + 1$ gives exactly the feasible locality masks of component-order deletion on P_q at cap k. For r disjoint $s \times s$ tables of unit records, take every row and column as a transaction. If*

$$C = (s-1)k + 1, \qquad s \geq \max\{2, k, \lfloor (k-1)^2/4 \rfloor + 2\},$$

then allowing rs shards of capacity C realizes every maximal allocation of r disjoint $K_{s,s}$ regions at cap k. The minimax expected locality regret is $\Theta(\min\{1, \sqrt{rk/m}\})$ after m transaction observations. The path instance inherits Eq. (6)*, with $d = q$ and without the quantum scale D.*

Proof. A run of a adjacent-pair transactions forces its $a+1$ records into one shard. Distinct selected runs have disjoint record supports. Thus the path masks are exactly the runs of at most k transactions.

In a table, any selected row and column share a record. A mixed selection of a rows and b columns must occupy one shard and contains $s(a+b)-ab$ records. If $a+b \le k$, this is at most $(s-1)k+1$. If $a+b \ge k+1$, a mixed subcollection of size $k+1$ has at least $s(k+1) - \lfloor (k+1)^2/4 \rfloor > C$ records. Monochromatic selections use separate row or column shards. These are precisely the biclique constraints.

Every maximal monochromatic selection uses s shards. A maximal mixed selection uses one shard for its union; the remaining records fit in at most $s-1$ further shards because $C \ge s$ and the union contains at least s records. Summing over regions proves feasibility with rs shards. Cross-region grouping cannot evade the within-region union bound. The optimum and empirical optimum therefore equal their component-order counterparts. The disjoint-region upper and lower bounds apply; locality regret is twice quantum prediction regret at $D = 1$. □

The strict capacity condition matters: $s = k = 5$, $C = 21$ also fits three rows and three columns, contradicting a cap-five interpretation. Increasing s grows transaction width, shard capacity and the server budget. The sample bound holds under this increase in storage resources. Independent enumeration checks 57,994 small tuple partitions, 28 path cases and 104,129 capacity comparisons.

M.1 Structured experiments and a public negative control

We use $r \in \{1,4\}$, $s \in \{4,8\}$, $k \in \{1,2,3\}$ and $m/(rk) \in \{4,16,64,256\}$. Each setting has 32 independent instances. A fixed full-support Dirichlet family and a separate budget-indexed paired-sign family test ordinary learning and worst-case scaling, respectively. Exact empirical maximization compares the row total, column total and largest k weights in each region. Every chosen mask is converted into an actual record placement, and locality is recomputed from its transaction footprints. All 15,360 such checks agree with the selected masks. Static rows, static columns, empirical color choice and a known-workload optimum use the same capacity and server envelope.

BenchBase continues the OLTP-Bench framework (Difallah et al., 2013). Its SmallBank generator uses uniform distinct account pairs; the pinned PostgreSQL sample assigns 40% of requests to two-account procedures (BenchBase contributors, 2025). We replay those footprints with 12 customer bundles and four shards of capacity three bundles, charging three logical records per bundle. Enumerating all 15,400 balanced packings gives locality $.6 + .4(2/11) = .672727$ for every packing. Every packing has the same locality, so learning cannot improve it. We replay the published generator's transaction footprints; we do not execute BenchBase or measure throughput.

M.2 Observed purchase baskets

The public Online Retail data contain 541,909 line observations (Chen, 2015). We retain positive-quantity, positive-price lines outside cancelled invoices, group distinct stock codes by invoice, and sort by timestamp. This gives 19,960 purchase baskets. We define an inventory workload that accesses the items in a basket; the data are observed purchases, not a captured SQL trace.

The first 3,992 baskets choose the most frequent 12 or 24 stock codes. The next 40% supply training requests, the next 20% train a validation comparator, and the last 20% form a common held-out trace. We project each basket onto the selected codes and score nonempty projections. The test denominators are 1,548 and 2,069 of the 3,992 final invoices. Oversized projections remain failures: 136 and 341 test baskets exceed the three-record shard capacity. Projection makes the optimization tractable but changes the task. It retains only 2.45% and 4.31% of test item incidences; just 10 and 23 original invoices lie wholly inside the selected catalogues. The reported locality therefore applies to these subcatalogues.

Each method uses exactly $n/3$ shards with three records each. A binary variable for every three-item block indicates whether that block is a shard; each item must appear once. Its weight counts training baskets contained in it. This set-partition MILP is exactly the empirical locality objective, including singleton baskets and the unavoidable failures larger than three items. All 128 fits (16 request streams, four budgets, two schemas) and both validation fits terminate with zero optimality gap. We use nested samples of $m \in \{8, 32, 128, 512\}$ requests from the training pool.

At 512 requests, mean test locality is 67.25% and 52.21% for the 12- and 24-item schemas, versus 63.57% and 48.19% for fixed frequency-ranked grouping. Fixed hash placement gives 62.08% and 47.70%. The validation-trained comparisons give 68.02% and 53.02% after 1,725 and 2,232 additional observed baskets. They are not population or test-selected oracles. Intervals resample the 16 training streams, conditional on the schema and the held-out trace. We do not assign an rk dimension to these general basket footprints.

M.3 Complete baskets on the full catalogue

We next retain all 3,922 stock-code identifiers and score every one of the 3,992 held-out invoices in full. We supply the catalogue as metadata, extracted retrospectively from the complete dataset. The learner knows the item identifiers but receives no future frequencies or co-occurrences. The experiment therefore tests allocation within a known catalogue. The chronological pilot/training/validation/test split is unchanged. Shard capacities are 128, 256 and 512 records. Every fitted and fixed method actually uses 31, 16 and eight shards, respectively, the minimum counts at those capacities. No method replicates records.

General basket partitioning is combinatorial. Our full-catalogue implementation searches five training-only candidates: four greedy transaction-merge orders and a pair-coaccess merge. Each merge obeys the record cap; first-fit decreasing packs the remaining components. The chosen candidate maximizes whole-basket locality on its training prefix. This is a heuristic, not an exact empirical maximizer. We evaluate $m \in \{8, 32, 128, 512, 2048\}$, with 16 nested request streams, yielding 240 fits. All footprint scores, capacities, shard counts, selected empirical objectives and training indices pass independent replay against the original public archive.

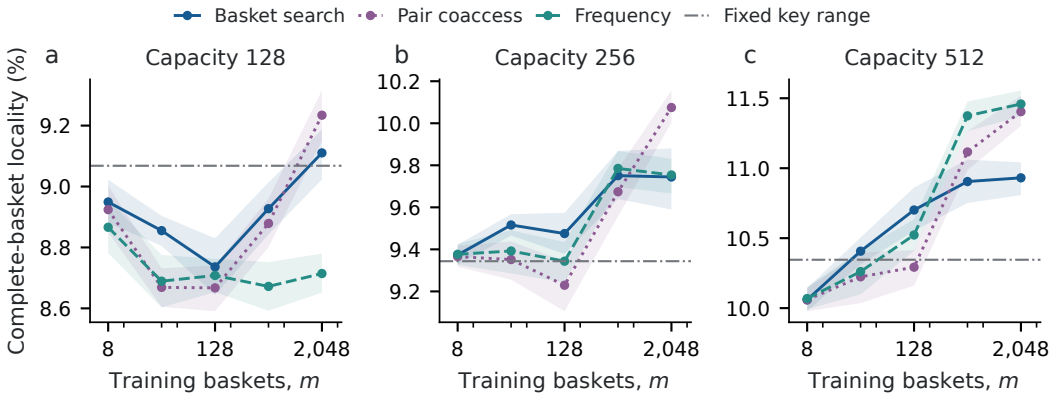

Figure 7: Complete-invoice locality on the full Online Retail catalogue. All three learned methods use the same training requests and actual shard count; fixed key range uses none. Pointwise 95% bootstrap bands resample 16 request streams, conditional on the fixed catalogue and held-out trace. Axes retain each capacity's local scale.

The frequency baseline ranks items by counts from the identical training prefix and groups consecutive items. We added this control after the primary study and retain its implementation and every output. At capacity 512, it beats basket search in 14/16 streams at $m = 512$ and 15/16 at $m = 2048$, by 0.470 and 0.528 points on average. At capacity 128, basket search instead has higher mean locality at every budget. The pair-coaccess candidate also exceeds the selected candidate on later data in some settings: selecting by training locality need not select the best future partition.

Independently pilot-ranked and validation-trained controls each consume 3,992 additional baskets and are charged separately. At capacity 512, their localities are 11.85% and 11.65%, compared with 10.35% for fixed key range and 7.57% for fixed balanced hash. The full study shows modest locality gains from observing requests, with the better method depending on capacity. It measures neither throughput nor latency.

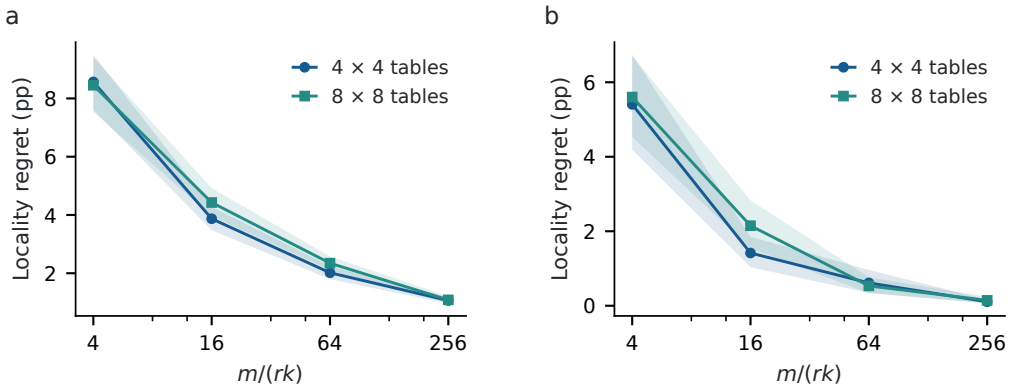

Figure 8: Structured classical transfer. (a) Budget-indexed paired-sign family; changing m changes the population. (b) Fixed full-support Dirichlet workloads. Curves average balanced cells in $r \in \{1, 4\}$ and $k \in \{1, 2, 3\}$, with 32 instances per cell. The horizontal scale is the proved $m/(rk)$; it is not applied to the public basket schema.

N Native 15-qubit path: execution and pending learning study

The data path is $(33, 39, 53, 52, 51, 58, 71, 70, 69, 78, 89, 88, 87, 86, 85)$ on `ibm_marrakesh`. We selected the path using backend calibration alone, before observing its experimental responses. Every one of the 15 queries is retained. Endpoint parity extraction uses three logical CNOTs. Internal queries use five CNOTs to fold parity toward an available ancilla and undo the borrowed-data transformation. Seven centers have physical degree two. Ideal Clifford identities verify the entire unitary, including restoration of arbitrary borrowed data; a separate binary-linear calculation verifies the parity map.

The request is fixed in each circuit. Preparation is compiled separately and has an identical prefix across requests for a given codeword. The compiled program therefore fixes preparation independently of the request, although the request is not generated late on the device. Both full and shallow graph states use even/odd CZ layers. We use native gates, active initialization, and no twirling, dynamical decoupling or error mitigation. Default-delay commissioning uses 250 microseconds between shots; the failed learning pilots used 25 microseconds. Those conditions are separate.

Job `dagas0hhvn6c73cqbhbg` returned 7,680 shots and charged five QPU seconds. Each of four fixed encodings has 64 shots per bit and query. We fixed the decoder before acquisition: it predicts the encoded bit directly from the reported parity. Full chain has 107 errors in 1,920 trials, fixed depth three 274, product even 481 and product odd 584. For the three simultaneous contrasts against Full chain, independent-shot Hoeffding bounds give depth-three minus full error 8.70 points, interval $[3.70, 13.69]$; even minus full 19.48, $[14.49, 24.47]$; and odd minus full 24.84, $[19.85, 29.84]$. These bounds assume independent shots within this fixed job. Request-learning variability and changes between device calibrations require separate acquisitions.

N.1 Frozen learning design and execution status

The request-only learner receives counts from $m \in \{8, 32, 128, 512\}$ requests and solves the depth-three ideal allocation problem. Four fixed full-support workloads are uniform, alternating, centrally concentrated and bimodal. There are 16 independent nested request streams per workload. The product comparator solves the depth-one problem on the same counts; Full chain uses every edge. A known-workload ideal depth-three comparator is privileged and is not the best unknown physical encoding. A separately calibrated learner at $m = 128$ varies $B \in \{4, 16, 64\}$ response trials per local context. It has additional observations and is never called request-only.

The planned 292,608-shot budget comprises 7,680 commissioning shots, 153,600 core comparisons, 46,080 calibrated tests, 57,344 calibration shots, 15,360 finite-catalog selection shots, 11,520 coherence controls and 1,024 input-bit controls. Core inference uses 16 separate request/acquisition blocks; the calibration arm has eight independent panels. Shared panels and response records must remain shared in resampling. The complete allocation list, workload probabilities, request prefixes, compiler and analysis plan are frozen in the artifact.

Two exploratory shared-response libraries were submitted before the confirmatory acquisition. Job `dagb0sj9k43c73ad42j0` planned 32,520 shots in 15,900 circuit publications; it timed out. Job `dagb5m8mhr3c73e4taag` retained every learned mask, used a stronger known-workload product comparator, and reduced the submission to 2,340 publications and 18,720 planned shots. It also timed out. Neither job returned usable observations, so neither contributes data to the learning curves. The supplement preserves the frozen circuits, receipts, error messages and usage records. The free-plan limit prevents completing the confirmatory learning and calibration curves in this revision.

The proposed success criterion is a positive paired advantage over both extremes on every workload at $m \geq 128$. We will evaluate this hypothesis on every workload and retain failures. A fixed-workload slope is descriptive: the minimax theorem does not predict $-1/2$ on every population. Any budget-indexed hard-family test must be labeled separately from learning a fixed workload.

N.2 A LIMITED COHERENCE CHECK EXPOSES A SIGN REVERSAL

Job `dagb9efi3e6s738m5tf0` returned 1,920 shots in 30 circuits, charging three QPU seconds. Every query has a coherent-extraction and local-refinement arm, each with 64 shots. This small diagnostic fixes the encoded bit and witness phase to zero; it does not cover both parity sectors or certify the all-input detector contract.

After extracting query K_i, we measure the neighboring commuting generator K_j ($j = i+1$, except at the last site). Ideal extraction preserves its signed expectation at one, whereas local refinement sets it to zero. There is no postselection. Direct parity parsing of the saved six-bit strings agrees with independent reversed-string parsing, and all QPY metadata match the returned circuit metadata. Exact Heisenberg propagation of the submitted native circuits verifies the complete 64-outcome ideal distributions. A separate ideal stabilizer simulation gives the same witness predictions. These checks concern the circuit specification, not the physical observations.

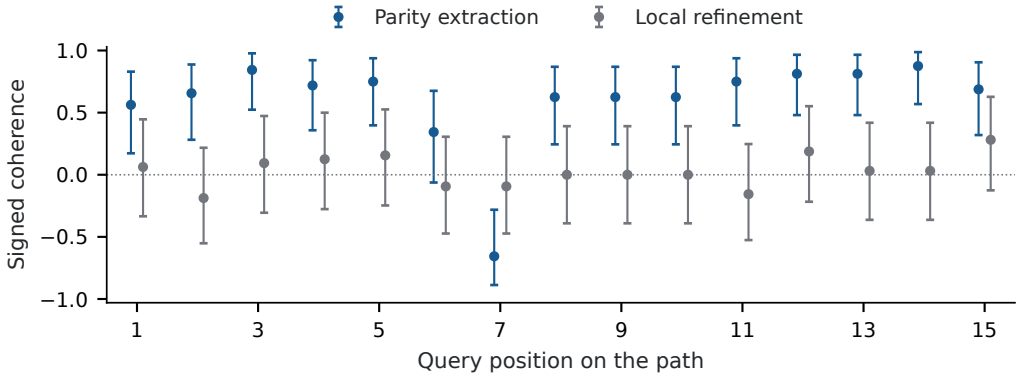

Figure 9: All 15 native-path coherence diagnostics. Bars are 95% simultaneous Clopper–Pearson intervals over 30 cells, conditional on independent shots. The query numbered seven reverses the expected sign; query six is inconclusive. No sign is selected from these data.

Mean signed coherence is 0.602 for extraction and 0.029 for refinement. Thirteen extraction cells have positive simultaneous lower bounds. Query six gives 0.344, interval $[-0.062, 0.675]$; query seven gives -0.656, $[-0.887, -0.282]$. The latter measures the witness on physical data qubits $(71, 70, 69)$. Its ideal value is positive, so the reversal remains an unexplained acquisition/device result. It rules out claiming that this check validates preservation across the whole path. The next

hardware stage must diagnose that cell and repeat both sectors and phases before attributing allocation performance to a coherence-preserving physical service.

N.3 The reversal repeats on both bits and witness phases

We used the remaining free allocation for a focused follow-up, selected after the preceding result. Job `dagbgdni3e6s738m65ig` returned 3,072 shots in 12 circuits, charging three QPU seconds. The selected query is tested at both encoded bits and both witness phases, with extraction, local refinement and a preparation-only witness reference. Each cell has 256 shots. The reference removes the extraction/measurement interval; it is not duration matched. The protocol, signs, circuits and all cells were frozen before submission. Ideal simulation of the exact submitted circuits again predicts signed coherence one for extraction and reference, and zero for refinement.

Table 3: Signed witness in the focused second job. Each value uses 256 shots. The query and follow-up were chosen after the first job; these are exploratory replication data, not a new confirmatory endpoint.

Encoded bit	Phase	Extraction	Refinement	Preparation only
0	0	-0.570	-0.016	0.914
0	1	-0.680	0.023	0.883
1	0	-0.664	-0.055	0.906
1	1	-0.688	0.117	0.875

All four extraction intervals are negative after Bonferroni correction over the 12 cells; their largest upper endpoint is -0.407. All preparation-only intervals are positive, with smallest lower endpoint 0.763; all refinement intervals contain zero. The sign reversal therefore repeats in a separate job over this input family. The comparison implicates the added extraction/measurement interval, including its timing, rather than preparation alone; it does not identify a specific faulty gate or distinguish measurement backaction from coherent evolution during the added interval. Both jobs use the same device and day. A duration-matched control and a separately frozen repair test remain necessary.

O Earlier prospective detector-service validation

The earlier three-data-qubit study uses qubits $(98, 111, 110)$ and ancilla 112 on `ibm_marrakesh`, with requests (ZZI, XXX, IZZ) at probabilities $(.2, .6, .2)$. Unlike the static 15-qubit commissioning circuits, it generates the request after preparation and executes the corresponding dynamic parity branch. Healthy operation is the native circuit. The fault adds an ancilla $R_y(2 \arcsin \sqrt{.15})$ rotation before the report; actual response probabilities are measured rather than identified with ideal flip rates.

Each of two cycles fits binary effects using 64 informationally complete product inputs per health hypothesis. Two continuous product searches produce candidate probes. A separate validation job measures eight candidates directly and selects a product and an entangled probe by estimated 32-report power. Both cycles select Z product and GHZ. These numerical searches do not certify the global physical separable optimum, and selecting GHZ does not show a gain from learning over fixed GHZ.

Scores and probes are frozen before healthy threshold calibration: 2,048 independent 32-shot episodes per primary policy, strict exceedance of order statistic 2,009. This targets a 2.5% false-alarm rate with 95.55% per-policy tolerance coverage under stationarity. Later jobs acquire 1,536 episodes per policy and health hypothesis. Each cycle must pass a one-sided Fisher superiority test at .025 and healthy one-sided 95% binomial upper bounds at most 5% for both policies. No pooled result rescues a failed cycle.

Both cycles pass the fixed aggregate rule. Conservative power-gap intervals are $[3.60, 14.58]$ and $[10.77, 21.83]$ points. However, GHZ alarms increase across jobs in the first cycle; its final job has 14/224 healthy alarms, or 6.25%. Aggregate control does not establish a stable future false-alarm rate. Both cycles share the device, layout and acquisition day. Observation separation is not independence of physical noise.

Table 4: Frozen prospective alarms. Each cell uses 1,536 original 32-shot episodes. Brackets are pointwise 95% binomial intervals under independent stationary episodes.

Cycle	Probe	Fault alarms (%)	Healthy alarms (%)
1	Selected product	30.53 [28.24,32.91]	1.43 [0.90,2.16]
1	GHZ	39.65 [37.19,42.15]	1.95 [1.32,2.78]
2	Selected product	29.82 [27.54,32.18]	1.69 [1.11,2.47]
2	GHZ	46.16 [43.64,48.69]	2.28 [1.59,3.15]

Fixed-query coherence controls cover both sectors and both phases for Bell and GHZ inputs, comparing extraction, destructive local refinement and a nominal idle channel. The idle is not duration matched. Two subsequent jobs test the actual dynamic branches: 56 target-request cells all have positive simultaneous lower bounds, with minimum signed coherence 0.302. No detector agreement or witness outcome selects the observations. These are finite-input witnesses, not an all-input instrument certificate.

The full earlier acquisition uses 1,482,496 shots and 522 charged QPU seconds in 40 jobs, including commissioning and coherence. Product, Bell and GHZ preparations use 0, 1 and 2 native CZ gates; the detector averages 4.2 CZs per call. Adaptive Z uses 1.6 logical calls and 6.0 CZs per trial, plus two physical report slots and reset overhead. Its thresholds use only 128 healthy episodes and a 5% target; its observed power is not comparable to the primary policies at a common operating rule. All eight candidates, secondary outcomes, job-level drift, gate counts, timing-payload discrepancies and raw provenance remain in the extended evidence supplement.

The earlier response-calibration study fits directly observed conditional binary probabilities. It does not identify the independent edge-error parameters of the theoretical preparation model. The extended supplement preserves that distinction and its full protocol.